DESIGNING AND TESTING AN EXPERIMENTAL PLATFORM IN SUPPORT OF PARTIAL GRAVITY TWO-PHASE FLUID PHYSICS MODELING

A Thesis

by

DANIEL VARNUM-LOWRY

Submitted to the Office of Graduate and Professional Studies of
Texas A&M University
in partial fulfillment of the requirements for the degree of

MASTER OF SCIENCE

Chair of Committee,	Bonnie J. Dunbar
Committee Members,	Moble Benedict
	Philip Hemmer
Head of Department,	Rodney Bowersox

May 2020

Major Subject: Aerospace Engineering

ABSTRACT

Several nations are on the eve of returning to the Moon, establishing permanent research stations, and utilizing the Lunar resources. Developing and experimentally validating two-phase fluid dynamic models for different gravitational regimes is critical for designing reliable Lunar and Martian hardware systems, to include human life support systems, cryogenic fuel management and in-situ resource utilization (ISRU). It is well known that in a microgravity environment, surface tension effects (liquid in contact with solid) dominate over buoyancy, whereas in most earth-based processes, buoyancy overcomes surface tension. The balance between these forces in partial gravity is relatively unexplored, and the instrumentation to measure these balances had not yet been developed.

This work presents the development of an instrument designed to measure the balance between gas buoyancy and surface tension in 1 g for a variety of liquids, gases, and solid surfaces. The experimental results from this instrument system are being compared to an independently developed CFD model, also developed in the Aerospace Human Systems Laboratory (AHSL). In the future, the CFD models will be extrapolated to variable acceleration environments, while the instrument will be designed to fit within a flight project on the International Space Station (ISS) to collect empirical data in artificial/altered gravity or, eventually, in a steady state $1/6^{th}$ g environment on the Lunar surface. Parametric empirical data will be compared with the CFD data to in order to generate future models. The experimental device is a custom designed and built, multi-axis, high-speed imaging system. The development, calibration, and validation of the imaging and gas injection systems have been completed and characterized. Experimental results are highly correlated with CFD models in 1 g. The instrument is accurate to within 3.52% when measuring the dimensions of a gas bubble, and repeatable to within 1.42% in bubble volume measurements.

DEDICATION

To my loving parents and sister: Susan, David, and Ciara

ACKNOWLEDGMENTS

I would like to thank the members of the thesis committee for carefully reviewing this thesis — especially Dr. Dunbar for supporting this research and encouraging me during my graduate studies. I also extend my gratitude to Dr. Benedict and Dr. Hemmer for being supportive committee members with valuable guidance and critiques. I would also like to thank the Aerospace Human Systems Lab (AHSL) and Department of Aerospace Engineering for supporting and furthering my education. I would especially like to thank doctoral candidate Paul Burke who worked countless hours by my side on this project.

CONTRIBUTORS AND FUNDING SOURCES

Contributors

This work was supported by a thesis committee consisting of Professor Bonnie J. Dunbar (advisor), Professor Moble Benedict of the Department of Aerospace Engineering, and Professor Philip Hemmer of the Department of Electrical and Computer Engineering. All work conducted for the thesis was completed by the student independently.

Funding Sources

This work was funded by the Texas A&M University Aerospace Human Systems Laboratory (AHSL) under Director Professor Bonnie J. Dunbar, and the generous support of the Chancellor's Research Initiative (CRI).

NOMENCLATURE

F_g	Gravitational Force
F_b	Buoyant Force
F_k	Kinetic Gas Force
F_i	Inertial Fluid Force
F_d	Drag Force
F_γ	Surface Tension Force
FOV	Field of View
$AFOV$	Angular Field of View
FL	Focal Length
WD	Working Distance
γ_{sg}	Solid-Gas surface tension
γ_{ls}	Liquid-Solid surface tension
γ_{lg}	Liquid-Gas surface tension
θ	Sessile drop contact angle
Φ	Free energy ratio
V_s	Molar volume of a solid
V_l	Molar volume of a liquid
Φ_x	Diameter along X-axis
Φ_y	Diameter along Y-axis
θ'	Bubble contact angle at detachment
AHSL	Aerospace Human Systems Laboratory

ISS	International Space Station
LEO	Low Earth Orbit
CFD	Computational Fluid Dynamics
NASA	National Association of Space and Aeronautics
ISRU	In-Situ Resource Utilization
MVP	Multi-use Variable Gravity Platform
TRL	Technology Readiness Level
ESA	European Space Agency
PIV	Particle Image Velocimetry
LDA	Laser Doppler Anemometry
ECLSS	Environmental Control and Life Support Systems
FARE II	Fluid Acquisition and Resupply Experiment Two
px	pixel
UNF	Unified Fine pitch threads
PC	Polycarbonate
Al	Aluminum
PTFE	Polytetrafluoroethylene
SiO_2	Silicon dioxide, quartz
H_2O	Water
N_2	Nitrogen
O_2	Oxygen
CO_2	Carbon Dioxide
Ar	Argon
GPIO	General Purpose Input/Output
I/O	Input/Output

RS-232	Recommended Standard 232
DC	Direct Current
FPS	Frames Per Second
f/	F-number
FR	Flow Rate
IPV	Incremental Pumped Volume
WT	Wait Time
T_d	Time of Bubble Detachment
ROI	Region of Interest
ESD	Equivalent Spherical Diameter
LED	Light-Emitting Diode
SF	Scale Factor
PE	Percent Error

TABLE OF CONTENTS

Page

LIST OF FIGURES

FIGURE Page

LIST OF TABLES

1. INTRODUCTION

1.1 Fluid Behavior in Reduced or Altered Gravity

When humans began to venture into the weightless, microgravity (10^{-6} g) environment of Low Earth Orbit (LEO), it was discovered that in two-phase (liquid-gas) systems, liquid surface tension dominated over buoyancy forces. Buoyancy is essentially zero in microgravity. Without buoyant forces, a number of spacecraft systems had to be designed differently. For example, forced air systems (e.g. fans) are required on spacecraft, such as the Space Shuttle and a variety of space stations, to circulate and mix physiological gasses (oxygen, carbon dioxide, and nitrogen) in order to support human health [1]. Astronauts had to be concerned about exhaling CO_2 which would saturate the air around them without any natural buoyancy driven gas exchange in the cabin. A "mission rule" requires that crews return to Earth for loss of all cabin fans. In addition, fuel systems are designed with innovative screens to manage and move liquids by taking advantage of surface tension forces [2].

However, gaseous bubbles, which can be produced through boiling and are advantageous in certain Earth gravity processes, have began to impede systems designed for microgravity. Bubbles block the delivery of fluids in medical intravenous (IV) systems and fluidic experiments [3][4] and have blocked liquid movement in experimental heat pipes [5]. Fluids research has been conducted in Earth's 1 g environment for thousands of years, with Archimedes' Principal of buoyancy dating to around 250 BC and microgravity fluids research conducted over the last six decades. Past experiments on sounding rockets, on parabolic aircraft, on the Space Shuttle, and on the International Space Station (ISS) have been directed toward the study of Marangoni flow, heat transfer, and bubbles, especially in the field of pool boiling [6][7]. Little to none fluid physics research has been conducted at gravity or acceleration levels representative of the Moon ($1/6^{th}$ g or 1.62

m/s^2) and Mars ($3/8^{th}$ g or 3.71 m/s^2). With very little existing experimental data, there are no predictive computational models and much debate as to the parametric relationship between gravitational levels and two-phase fluid behaviors.

1.2 Statement of Work and Motivation

The focus of the Aerospace Human Systems Laboratory (AHSL) research is to understand buoyancy in a partial gravity environment, particularly bubble generation or nucleation, and the subsequent relationship between the forces of gravity/buoyancy and surface tension when bubbles are attached to a solid surface. This knowledge is fundamental to designing hardware systems such as life support systems, for in-situ resource utilization (ISRU), or for basic research on the Moon ($1/6^{th}$ g) or Mars ($3/8^{th}$ g). No computational fluid models exist for predicting fluid behaviors in reduced gravitational environments because there is no experimental data from which to draw. In order to gain some insight into the balance between surface tension and buoyancy, and where the transition in dominance might occur as a function of the magnitude of the gravitational force, the AHSL is focusing on bubbles, specifically the balance of buoyant and surface tension forces.

Although industry has been studying bubbles for decades as they relate to heat and mass transfer, or chemical reations, most of those studies were focused on the bubble after it separated from a surface and was in motion. However, it is known from microgravity research with pool boiling, in the absence of buoyancy, that the bubbles never detach, but remain attached to where they nucleate [6]. Bubble behavior between 1 g and microgravity is not known and there is limited research on the dynamics of bubble formation and separation as a function of gravity. There continues to be debate within the scientific and engineering community on the parametric relationships —at what level is the transition from surface tension to buoyancy? How do materials of different surface energies affect both nucleation and bubble separation under varying gravitational environments? What are the effects of varying the liquids and gas compositions as well as temperature?

For the research hypothesis being investigated by the AHSL, there exists no known research instruments designed to specifically study bubble formation and surface separation due to buoyant forces, and how that separation is affected by material surface energies, the composition of the gas and the liquid, and other variables. Therefore, the purpose of this thesis is to design and test an experimental platform for the purpose of investigating the balance between buoyant and surface tension forces on a gas bubble in a liquid. An experimental platform is needed to measure bubble volume and contact angle on a substrate at the point of bubble detachment or the point at which the force of buoyancy overcomes the force of surface tension. This instrument should be designed to obtain data in 1 g. The experimental data collected from this laboratory instrument will be used to validate 1 g computational fluid dynamic (CFD) models developed by the AHSL. The concurrently developed CFD models must then be validated with experimental data. The thesis work should provide preliminary design considerations and trade spaces for a space flight experiment. A possible spaceflight opportunity is provided by the Techshot Centrifuge on the ISS. AHSL is also currently exploring experiments deployed to the Lunar surface. Experiments conducted in artificial or steady state partial gravity will form a much-needed empirical data base for reduced gravity CFD validation.

1.3 Two-Phase Fluid Systems in Earth Gravity

Liquid-gas two-phase fluid systems are used in a wide array of applications. They are commonly found in chemical, nuclear, petroleum, biomedical, and environmental engineering applications. Two-phase fluid systems are noteworthy for their superior power and mass saving capabilities in mass and heat transfer applications [8]. From heat pipes to nuclear reactors, two-phase fluids are found in some of the most important systems on Earth and in space [9][10]. Research into two-phase fluids in the chemical, nuclear, and petroleum industries typically focuses on pool boiling, pipe flows, and phase separators since these are the most common terrestrial use cases. Two-phase fluid systems are comprised of a liquid phase and a gaseous phase that are distributed in several distinct ways.

The dispersion of gases in liquids is often described as the flow regime. As mentioned previously, most research has been concerned with pool boiling and pipe flow. In pipe flow there are five types of flow regimes: bubbly, coring bubbly, slug, churn, and annular (shown in Figure 1.1). The differences in these flow regimes are clearly visible, ranging from bubbly to annular flow. The void ratio (the gas to liquid ratio) increases as the flow transitions across regimes from left to right (excluding coring bubble flow) [11][12].

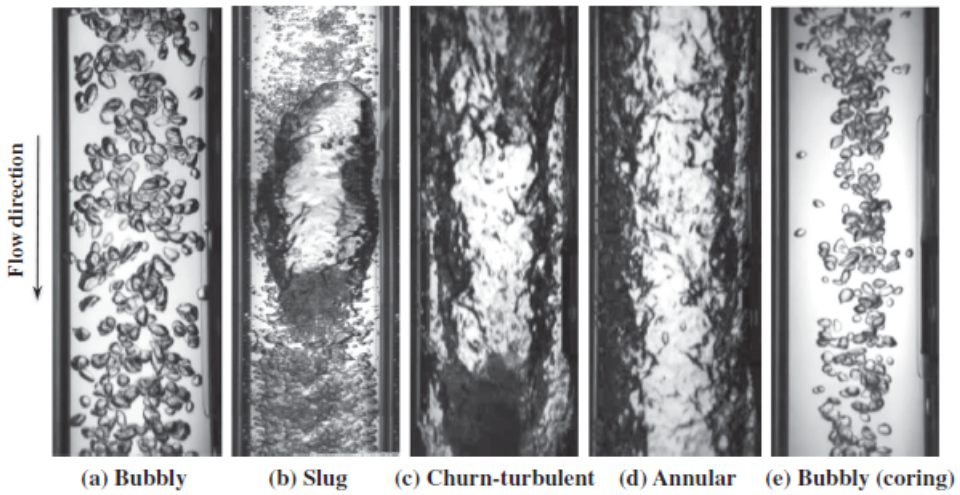

Figure 1.1: Two-Phase Pipe Flow Regimes. Reprinted from Qiao, 2017 [11]

Understanding the different types of two-phase flows (pipe flow and pool boiling, to name a few) and their respective flow regimes is critical for designing robust two-phase fluid systems; however, a system designed to operate in one gravitational regime might suffer severe performance degradation or fail entirely in another gravitational regime. System failure has been observed in a number of two-phase fluid systems, terrestrially and in space. This has been the case in microfluidic experiments in space were bubbles have blocked microchannels, compromising and/or terminating the experiments [4]. Bubble blockages have also been observed in experimental heat pipes on the Space Shuttle [5]. It is certainly important for these and other systems to operate as expected in order

to not waste money and risk mission failure.

1.4 Gravity and Buoyancy

On the surface of the Earth, the acceleration due to gravity is often considered to be a constant (e.g. 1 g). Equation 1.1 shows the equation for the force of gravity F_g acting on an object, where g = 9.8 m/s^2 on Earth and m is the mass of the object. Buoyant forces are related to the gravitational force. Equation 1.2 shows the equation for the buoyant force F_b acting on an object, where V_s is the submerged volume of the object, ρ is the density of the fluid the object is submerged in, and g is the gravitational acceleration (Earth = 9.8 m/s^2). On Earth, buoyancy drives chemical processes, cooling/heating, and the weather.

$$F_g = m * g \tag{1.1}$$

$$F_b = V_s \rho g \tag{1.2}$$

1.5 Balance of Forces: Buoyancy and Surface Tension

There is no known work which explores the balance of surface tension and buoyancy for a number of experimental variables: gravitational level, surface energy of a solid, composition of the liquid, composition of the gas, and temperature. In order to begin to develop the experimental data base, it is necessary to conduct controlled experiments first in 1 g, which can be compared to the CFD models.

The experimental model selected is the growth of a gas bubble in liquid on a solid plate. Bubble formation and detachment at an orifice has been studied for decades, including the quiescent case of low flow rates [13]. As the gas bubble volume increases, so does the buoyant force. Then the gas flow rate is very small, the buoyancy and surface tension are the only significant opposing forces, as shown in Figure 1.2. The forces that are insignificant in the quiescent case include kinetic gas forces, inertial fluid forces, and drag forces (F_k, F_i, and F_d). Consequently, the bubble detaches when the buoyancy force exceeds the surface tension force ($F_b > F_\gamma$).

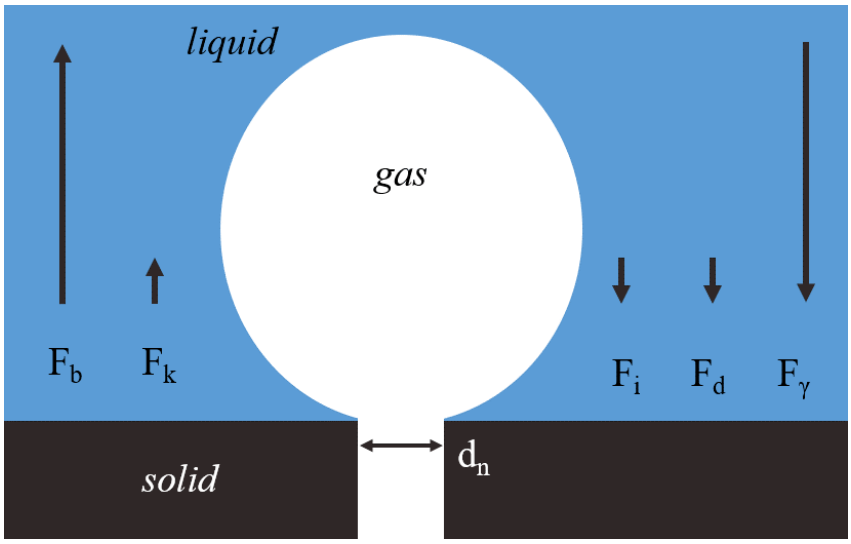

Figure 1.2: Forces Acting on a Slowly Growing Gaseous Bubble at an Orifice in a Liquid with Arrows Indicating Magnitude and Direction

1.6 Instrument Design Requirments/Objectives

The primary objective of the laboratory experiment for which this instrument was designed is to measure the volume of a given gas at precisely the moment it detaches due to the buoyant force from a given substrate with a given surface energy. This is the "balance of forces" between surface tension and buoyancy. Concurrently, a separate project in the laboratory is developing a CFD model with the same variables. The objective of the CFD model is to replicate the experimental results. With confidence in the 1 g experiment and the corresponding model, the CFD model can then be extrapolated to variable gravity environments such as those found on the Moon and Mars. However, the CFD results at less than 1 g still require experimental validation. In order to ensure accuracy of the CFD model at 1 g (Earth), so that the model may be extrapolated with only the gravitational level as the variable, it is critical that the 1 g instrument accurately calculate the gas volume at separation, that all other forces except buoyancy are controlled or negligible, and that the surface energies of the substrates are well characterized. Specific design requirements are listed in Table 1.1

Table 1.1: Two-Phase Fluid Experimental Platform Design and Research Requirements

Requirements	**Solution-Neutral Problem Statement**
Design Quiescent Bubble Detachment Experimental Platform	• Design a fluid container • Design a slow gas bubble forming system • Characterize the surface energy of solid substrates from low surface energy to high surface energy
Measure Bubble Parameters	• Design measurement system for capture of gas bubble interface (contact angle) geometry during detachment • Design a system for accurately measuring volume and dimensions of gas bubble at detachment
Develop Experiment Control Code	• Develop experiment control software for bubble formation • Develop experiment control software for capture of bubble interface geometry during detachment
Develop Analysis Code	• Develop analysis software for captured interfacial bubble data
Conduct Experiments and Analyze Results	• Conduct bubble detachment experiments over a variety of test parameters, from low to high surface energy substrates • Analyze captured interfacial bubble data, including statistical accuracy and repeatability

The scope of this thesis does not include development of the CFD models, which are being developed by PhD students in the AHSL. Rather, the scope of this thesis project is to develop and test an experimental platform for the purpose of future model validation.

In addition, the laboratory-based instrument will be used to increase the technology readiness level (TRL) for planned flight experiments. Based on the experimental configuration designed in this thesis project, flight experiments will be conducted in artificial partial gravity inside a centrifuge on the ISS. The Techshot Inc. Multi-use Variable Gravity platform (MVP) [14] is a potential future partner for the flight experiment phase of the continuing lab research. Conducting the simple two-phase bubble experiment onboard a centrifuge will provide researchers with critical relationships between bubble parameters and gravity levels. Furthermore, the data captured by the flight experiment can then be used to validate two-phase CFD models in partial gravity.

2. LITERATURE REVIEW

2.1 Bubble Detachment Studies

A number of studies have been conducted that examine the physical processes involved in bubble detachment. Reviews of these experiments have been compliled by Kumar [8] and Kulkarni [15] in 1970 and 2005, respectively. These review papers cover the wide range of variables that affect bubble detachment processes. These studies include investigations into surface tension and buoyancy in 1 g. A review of the limited research on the effects of the gravity level was also discussed, but none of the reviewed papers investigated the relationship between buoyant forces and surface tension forces in reduced gravity. From these reviews it is clear that there is a gap in understanding the "balance of forces" between surface tension and the buoyancy over variable gravity levels.

The most analogous study that has been found in the literature was the drop tower experiment conducted by Tsuge in 1997 [13]. Tsuge's reseach investigated the surface tension relationship with the gas momentum force in a low gravity environment (10^{-3} g). In this experiment a pressurized nitrogen chamber and a control valve were used to inject gaseous nitrogen into a liquid solution (water or methanol) through a 1.99 mm orifice. Tsuge also developed an analytical model for bubble detachment at variable gravity levels, but only 10^{-3} was tested experimentally. It was found that for low flow rates, bubbles did not detach in the 10 seconds of free fall provided by the drop tower. Where Tsuge compared the kinetic forces on a bubble to surface tension, we intend to do the same with buoyant forces over variable gravity levels.

Another similar experiment was conducted by Herman in 2002 on NASA's KC-135 parabolic aircraft [16]. This experiment examined bubble detachment from an orifice in variable gravity under the influence of electric fields. Rather than examining bouyancy

driven detachment processes, Herman focused mainly on the effects of electrohydrodynamic forces. The experiment setup included a 9 cm x 9 cm x 10 cm fluid chamber with a top and bottom electrode, a syringe air injection system, and a video camera for recording bubble behavior. The air injection orifice was located on the bottom electrode and was 1.5 mm in diameter. A constant flow rate was used for this experiment.

A bubble detachment experiment was conducted by Nahra to study the effects of fluid cross flow on bubble formation in low gravity in 2000 [10]. This experimental instrument used a syringe pump to form a gas bubble at an orifice. The diameters of orifices that were tested were 0.33 mm and 0.76 mm. The gas injection rate used in this experiment was 8 mL/min (133 μL/s). This experimental was flown on a DC-9 parabolic aircraft and was tested at a variety of gravity levels between 10^{-3} g and 1 g [10]. Similar to Tsuge and Herman, this study relied on constant flow rates. Consequently, the study was more focused on the balance of momentum and surface tension forces than the balance of buoyant and surface tension forces.

2.2 Imaging and Measurement Systems for Two-Phase Fluids

The observation and measurement of two-phase fluids uses several different techniques [15][8]. These techniques are broadly split into two categories: noninvasive and invasive. Noninvasive techniques do not disturb the fluid flow and include high-speed photography [16][17][18], particle image velocimetry (PIV) [19][20][21][22], laser doppler anemometry (LDA) [23], and tomography [24][25][26][27]. Invasive techniques do disturb the fluid flow and include methods such as optical probes and hot-wire probes [15]. Invasive techniques are less prevalent since they create their own disturbances in the fluid flows. For this reason, only non-invasive imaging techniques will be discussed further.

2.2.1 High-Speed Photography

The most common method for imaging two-phase fluids is high-speed photography [15]. This approach has excellent spatial resolution but is less useful for flows with multi-

ple, discontinuous bubbles [15]. Typically, high-speed camera methods rely on computer vision algorithms to detect and measure bubble properties (volume and contact angle) [28]. These algorithms are highly accurate for single bubbles but become less accurate with greater numbers of bubbles. This loss in accuracy is the result of bubbles that overlap in the cameras field of view: overlapping bubbles often cannot be properly measured [20].

2.2.2 Particle Image Velocimetry

The PIV approach is capable of capturing turbulent and multi-bubble flows because of its superior time resolution [15][19][20][21]. PIV imaging requires seeding particles, a laser sheet, and one or more specialized CCD cameras [22]. The seeding particles are introduced into the fluid to be observed (either the gas phase or the liquid phase). The laser is then used to excite these particles which is detected by the camera. However, this approach has a drawback, single-camera PIV systems can only capture fluid flows in a single 2D plane. Stereoscopic and tomographic PIV systems exist, but they are complex and expensive [22]. The high time resolution and particle tracking capabilities provided by PIV approaches are not necessary when imaging quiescent flows; instead bubble shape, volume, and contact angle are more desired. High speed imaging is capable of capturing these parameters.

2.2.3 Laser Doppler Anemometry (LDA)

LDA systems provide equally high time resolutions as PIV systems, making them another common method for measuring high speed flows with multiple high velocity bubbles [15]. LDA systems work by measuring the frequency shift of scattered light that collides with a moving particle [29]. This frequency shift can be used to calculate the velocity of the scattering particle. LDA systems, however, only acquire velocity information. Bubble shape and contact angle cannot be collected using this method. Furthermore, LDA is restricted to low void ratios (the volume of gases to the volume of liquids) due to large

refractive index gradients [19]. The advantages provided by LDA, like PIV approaches, are not necessary for imaging single quiescent bubbles.

2.2.4 Tomography

Another category of noninvasive methods for fluid imaging is tomographic imaging. Tomography utilizes penetrating waves to image 2D slices of a fluid [15]. This method requires the image to be reconstructed through a complicated computational process [25]. The images produced by this method are capable of collecting important two-phase flow parameters such as the void ratio, but they lack the spatial resolution to accurately describe a single bubble shape [24][25][30][31]. Tomographic techniques are most commonly used in medical applications since they offer a noninvasive imaging capability for soft tissues. One type of tomographic imaging, electrical impedance tomography, works well on soft tissues because the resistivity contrast in tissues is usually less than an order of magnitude [27]. However, the resistivity contrast in two-phase fluids is three orders of magnitude [27]. Current image reconstruction methods for high contrast systems show poor performance [24]. Other tomographic systems include electrical capacitance tomography [25][26] and X-ray imaging [15][8]. The current state of the art for tomographic imaging is not capable of accurately reconstructing spacial information for two phase flows.

2.3 Model Validation

Numerical model validation is accomplished through the acquisition of empirical or experimental data. Acceptable numerical models are dependent upon the accuracy, repeatability, and quality of measured data for a given set of variables. Well designed models can then be used to predict system and variable behaviors outside of the measured data set. For this reason, validated numerical models are being used to predict air and spacecraft behaviors for which there is no test environment. The development of two phase fluid models in altered gravity will be critical to the design and development of Lunar and Martian environmental control an life support systems (ECLSS), cryogenic

fuel management systems, and in-situ resource utilization (ISRU). Past CFD models for fluids in microgravity, such as static meniscus shape, have been validated through tests that were conducted in the FARE II flight experiment on Space Shuttle [32]. Simple flight experiments were used to collect data on fluids in microgravity, starting on a Mercury flight, continuing on the Space Shuttle, and now on the ISS [32]. These experiments have included static meniscus shape, tank inflow, and surface tension driven convection [32][6]. With the data gathered from these benchmark tests, fluid physics researchers are beginning to be able to validate their CFD models.

2.4 Studies on the Effects of Gravity on Liquid Behavior

The most frequently utilized ground based analogs for reduced gravity fluids research are drop towers, parabolic flights, and sub orbital flights [13][16][33][34][10]. Another research platform that is used to investigate the effects of gravity on fluids is centrifugation [34]. Each one of these methods have advantages and disadvantages depending upon the type of two-phase fluids experiment being conducted. Some methods present issues that are unresolvable for the proposed bubble-orifice experiment, while others only pose minor challenges. The following discussion summarizes these various methods and assesses their potential application to the bubble formation project.

2.4.1 Drop Tower Tests

A drop tower test utilizes a vertical vacuum tube that can be hundreds of meters tall. These facilities allow experiments to be conducted in free fall for short periods of time. The Japan Microgravity Center drop tower (now decommissioned) provided near weightlessness for around 10 seconds maximum [13] and was 710 m long. The NASA Zero Gravity Research Facility drop tower provides only 5.2 seconds and is 132 m long [35]). In 1997, Tsuge used the drop shaft at the Japan Microgravity Center to investigate bubble formation under reduced gravity [13]. This experiment examined the effects of gas flow rates on bubble formation and detachment in this 10 second drop tower and found

that bubbles did not detach in the low gas flow rate range. Under these conditions, a 10 second formation time was not long enough to observed detachment, if it were to occur at all [13]. These results indicate that the short time-frame for drop tower experiments is disqualifying when conducting quiescent fluid experiments.

2.4.2 Parabolic Flight Tests

Experiments conducted in parabolic flights and suborbital flights utilize the same free fall principal used in drop towers. Parabolic flights can provide acceleration levels between 2 g and 10^{-3} g for a period of about 20 seconds [16][33][10]. Suborbital flights are capable of about the same gravity levels but for a period that lasts many minutes. The 20 second reduced gravity time periods achieved in on board aircraft such as the NASA DC-9 and the NASA KC-135A (shown in Figure 2.1) are still quite short for conducting quiescent fluid experiments. In addition, all KC-135A flights ended in 2004 [36], but the DC-9 continued to fly until 2015. The longer periods achieved on sub-orbital flights hold greater promise for quiescent bubble detachment experiments, but only if the gravity level can be maintained at a given level.

Figure 2.1: NASA's KC-135A Parabolic Aircraft. Reprinted from Petty, 2004 [36]

2.4.3 Partial Gravity Centrifuge Tests

A method used to study the effects of gravity on fluid systems is centrifugation [34]. Centrifuge facilities are capable of producing an artificial force outward from the center of rotation. This centrifugal force, generated by a rotating reference frame, is also called artificial or altered gravity. This method of studying gravity has been used both in Earth's gravity and in microgravity in LEO. The benefit of conducting a centrifuge experiment in LEO is that the effects of Earth's gravity are reduced to 10^{-6} g. Results obtained through this method, however, are complicated by the Coriolis effect. Centrifuge experiments have been conducted in space as early as 1985 on the German Spacelab Mission D-1 [37]. Figure 2.2 shows the Techshot Multi-use Variable Gravity Platform (MVP) centrifuge on board the ISS.

Figure 2.2: Techshot's Multi-Use Variable Gravity Platform (MVP) on board the International Space Station (ISS). Reprinted from Techshot, 2019

2.5 Summary (State of the Art)

The rapid development of imaging systems, microprocessors, computer vision algorithms, and spaceflight hardware has allowed for an increased number of fluid flight

experiments. These experiments have been a driver for better understanding of fluid systems and many other systems in space applications. CFD models pose a cost and time saving solution to running experiments for every spaceflight fluid system, but these models require validation. Currently, no validated CFD models exist for bubble formation and detachment at an orifice in partial gravity due to a lack of experimental data. The AHSL's fluids research group has begun preliminary development of a bubble detachment model. The experimental platform that was designed for this thesis project will be used to validate the model in 1 g.

The selected approach for a future quiescent bubble detachment experiment was determined based upon advantages and disadvantages of each technique discussed previously. Drop towers are capable of achieving reduced gravity but cannot maintain this environment beyond a few seconds. Parabolic flights and suborbital flights are also capable of providing a reduced gravity test environment. The reduced gravity periods for a parabolic flight is only 20 seconds and the period is on the order of minutes for suborbital flights. It is not known if these time periods are long enough for bubble detachment at reduced gravity levels. Another viable option for (artificial) reduced gravity was centrifugation. An accurate quiescent bubble detachment experiment can be conducted in a centrifuge on the ISS. The only other promising option is to conduct experiments in steady state reduced gravity environments such as on the Lunar surface. For a ground based system, as described in this thesis, a high-speed camera was selected for the imaging method based upon the excellent spatial resolution and relative simplicity. Other approaches, such as PIV and LDA are feasible but are also too complex for this application. Tomographic techniques are not currently robust enough to be used for small bubble volume measurements.

Multiple references were consulted when designing systems for the experimental instrument in this thesis. Kumar [8], Kulkarni [15], Tsuge [13], Herman [16], and Nahra's papers [10] were especially useful for comparison with past bubble experiment designs.

However, no previous experiment has been designed for the purpose of studying quiescent bubble detachment from various orifice substrates utilizing multi-axis imaging.

3. METHODOLOGY

3.1 Approach

The objective of this thesis project was to design and test an experimental platform for the purpose of collecting volumetric and contact angle data on bubble formation, growth, and detachment at an orifice in 1 g. (Note; bubble rise is outside the scope of this project). Table 3.1 provides the complete list of system design requirements. These requirements define the necessary criteria for the experimental platform that must be met in order for the project to be considered complete and acceptable for collecting empirical data. Table 3.2 summarizes the development stages of this design project from Initial Research to Testing and Analysis.

Table 3.1: Two-Phase Fluid Experimental Platform Design Requirements

Requirement Number	**Requirement Name**	**Definition**
R1	Fluid Chamber Clarity	Clear polycarbonate with low distortion
R2	Fluid Chamber Dimensions	A minimum interior volume of 40 mm x 40 mm x 40 mm
R3	Incremental Gas Pumping Volume	Gas must be capable of being pumped at incremental volumes down to 0.1 µL
R4	Gas Pumping Rate	Gas must be capable of being pumped at flow rates from 0.1 µL/s to 1 mL/s
R5	Working Fluids	Distilled water and air to be used as the two fluids, with the capability to switch to other fluids
R6	base plate Swapping	base plates should be interchangeable
R7	base plate Materials	base plates should have a range of surface energies
R8	Camera Frame Rate	Cameras should capture at a minimum of 250 FPS
R9	Number of Cameras	A minimum of 2 cameras
R10	Lighting	Sufficient lighting to capture bubble images without additional ambient light
R11	Volume Measurement	Imaging system shall be capable of measuring gas volume at detachment

Table 3.2: Development Stages for the Two-Phase Fluid Experimental Platform

Development Stage	**Decision-Making Process**
Initial Research	Assess Research Gaps • What is the current state of the field? • What are the research opportunities?
Concept	Generate and Refine Concept for Experimental Platform • What should the requirements be? • What are the research goals and scope? Determine Possible System Architectures • What are the system level design choices? • Which architecture should be pursued?
Development	Design Subsystems • What subsystems are needed to achieve the desired system architecture? Select Components • What components are optimal (cost and schedule) for each subsystem? Design Test and Evaluation Procedures • What experiments should be conducted? • What safety requirements are needed?
Manufacture	Construction of Experimental Platform • What is the schedule for fabrication of components? • What assembly will take place in-house?
Testing and Analysis	Conduct Experiments • What logistics are associated with conducting experiments? • What problems are encountered during experiments? Analyze Results • What do the results show? • What do the results not show?

The design project was further divided into two chronological phases: Phase 1 and Phase 2. This was an iterative design approach wherein the Development, Manufacture, and Testing stages were repeated sequentially (first in Phase 1 and then in Phase 2). The selected components for these phases are provided in Table 3.3.

Table 3.3: Selected Components for Experimental Development Phases 1 and 2

Phase Number	**Selected Components**
Phase 1	First Iteration of Fluid Chamber • 45 mm x 45 mm x 58 mm extruded polycarbonate walls • Polycarbonate bottom plate • 1.6 mm orifice diameter Pumping System • LEGATO 110 series infusion pump • 20 mL Harvard Apparatus gastight syringe • ASCO 411 series 3 way normally closed solenoid valve Single-Camera Imaging System • 1 Daheng Imaging MER-031-860U3M camera • 920 FPS
Phase 2	Second Iteration of Fluid Chamber • 50 mm x 50 mm x 115 mm polycarbonate sheet walls • Exchangeable bottom plates (polycarbonate, Teflon, aluminum, and quartz) • 0.8 mm orifice diameter Pumping System • LEGATO 110 series infusion pump • 20 mL Harvard Apparatus gastight syringe • ASCO 411 series 3 way normally closed solenoid valve Multi-Axis Imaging System • 2 or 3 Daheng Imaging MER-031-860U3M cameras • 920 FPS

In Phase 1 of the project, a simplified experiment was designed and tested to determine the most sensitive experimental and design parameters. In Phase 2, the instrument design was optimized based upon the information obtained in Phase 1. The Phase 2 design was determined to be the final design configuration for this thesis design project.

3.1.1 Experimental Design Methodology

The experimental instrument was designed with three major systems/categories: (1) the passive components, (2) the pumping system, and (3) the imaging system. Figure 3.1 shows the three major systems and their constituent parts. The methodology for selecting components for each of these systems is provided in the following subsections. The general procedure for selecting a design for a system was to first create a notional de-

sign based upon similar experiments found in literature, then to conduct a trade study of the potential components, and finally to purchase and assemble the systems. Figure 3.2 shows the CAD model of the notional Phase 2 experimental apparatus. Discussion of the experimental parameters evaluated in Phase 1 and Phase 2 is included in Sections 3.2 and 3.3.

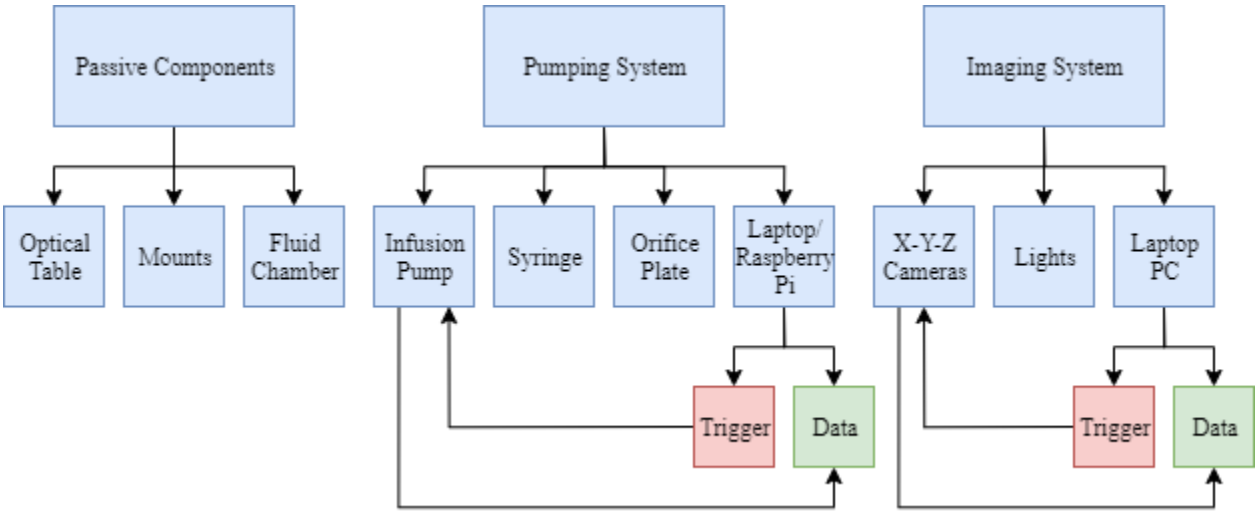

Figure 3.1: Experiment System Architecture

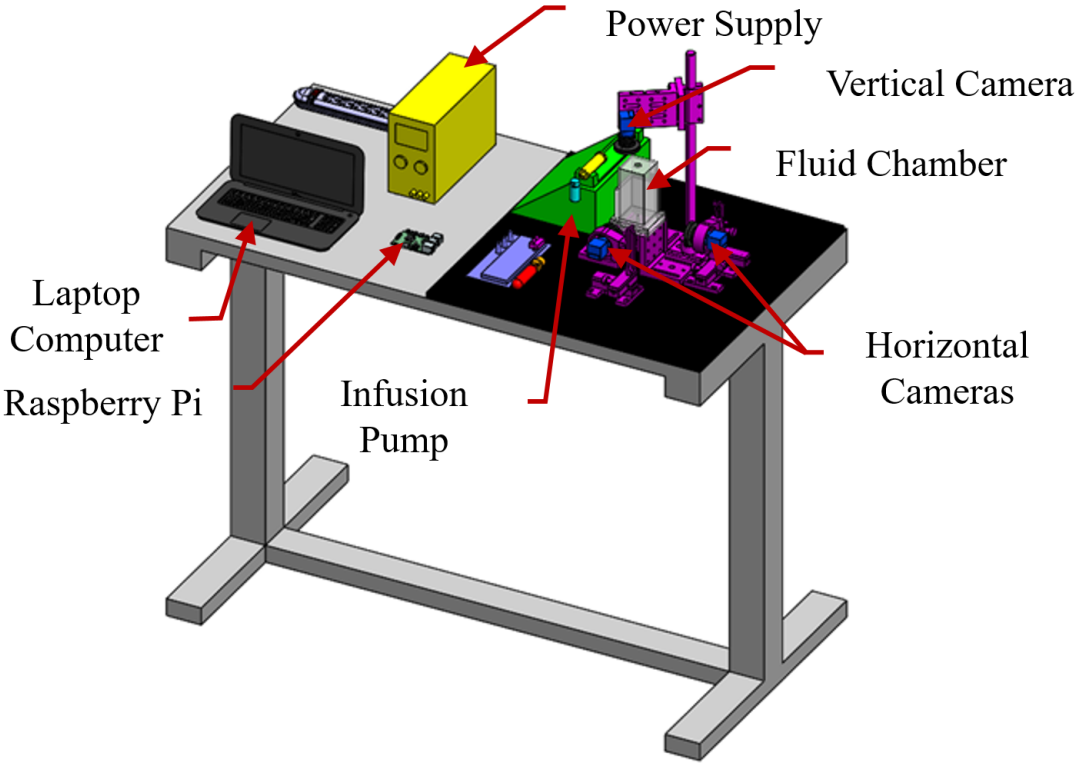

Figure 3.2: CAD Drawing of the Phase 2 Experimental Platform

3.1.1.1 Passive Components Trade Study

Passive components consist of the optical table, the fluid chamber, and the mounting hardware. Passive components are not powered and are static in their intended operation. A lab bench was used as a workstation for all of the experiment components. Mounts for the fluid chamber and imaging system are included as passive components. These pieces of hardware are used to affix camera and fluid chamber components that should not be accidentally shifted. The fluid chamber for the experimental apparatus is a transparent vessel for containing the liquid phase of the experimental fluids. The fluid chamber requirements, R1, R2, and R5, are shown in Table 3.1. Two iterations of the fluid chamber were designed to meet the fluid chamber requirements: one for Phase 1 and a second for

Phase 2. The final designs of this system for Phase 1 and Phase 2 are discussed in Sections 4.1.1.1 and 4.1.2.1, respectively.

3.1.1.2 Pumping System Trade Study

The pumping system was designed to pump gas from a reservoir, through tubes and valves, and into the fluid chamber. Figure 3.3 shows the pumping system block diagram. Five requirements for the pumping system include R3−R7. A trade study was conducted to determine the availability of components that could meet these five requirements. Both phases utilized an infusion pump with a gastight syringe. The syringe was connected to the fluid chamber orifice through a series of pipes, valves, and fittings shown in Figure 3.3. The pumping system tubing was connected to the bottom plate of the fluid chamber as shown in Figure 3.4. An base plate was bonded to the top of each bottom plate and sits directly on top of the air-injecting tube. The base plate reduces the cross-sectional area to the final orifice diameter for bubble injection. The addition of a removable bottom plate in Phase 2 allowed the fabrication of multiple base plates. The Phase 1 and Phase 2 final designs of this system are discussed in Section 4.1.1.2 and 4.1.2.2, respectively.

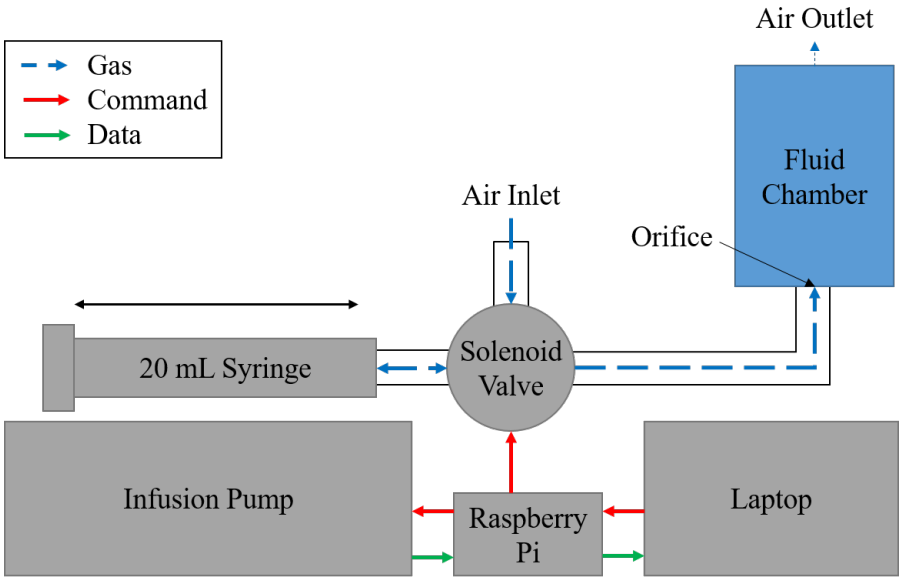

Figure 3.3: Pumping System Block Diagram

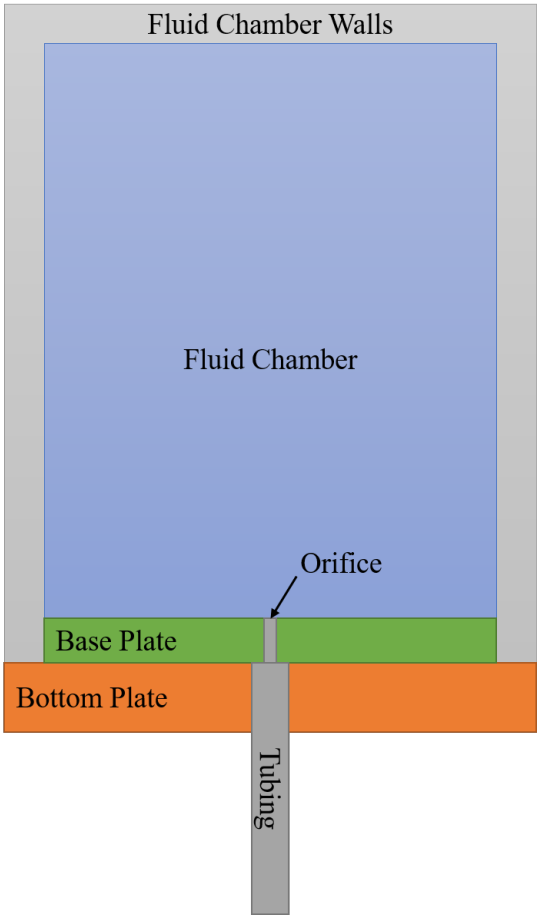

Figure 3.4: Bottom Plate, Base Plate, and Fluid Chamber Assembly

As indicated in Figure 3.1 and Figure 3.3, the pumping system is controlled by a laptop computer and Raspberry Pi. The laptop and Raspberry Pi work in a master/slave configuration where the laptop commands the Raspberry Pi to execute specific commands to the peripheral equipment. The Raspberry Pi is needed to interface with the infusion pump and the solenoid valve. The solenoid is powered by a DC power supply.

3.1.1.3 Imaging System Trade Study

The imaging system was designed to capture the bubble shape (the contour of the liquid-gas interface) during formation, growth, and detachment. The requirements that this system was designed to meet, R8−R10, are listed in Table 3.1. A trade study was

conducted to evaluate the available commercial options. The high-speed camera market has a wide variety of options with many different price points. The imaging system for Phase 1 used only one high-speed camera and relied upon an axisymmetric assumption to calculate bubble volume. The Phase 2 imaging system was developed to use either two or three high-speed cameras on mutually orthogonal axes.

The camera-lens system was selected based upon the field of view (FOV) calculated using Equation 3.1 and Figure 3.5, where AFOV is the angular field of view in degrees. A minimum of a 20 mm FOV was determined based upon bubble diameters reported in literature.

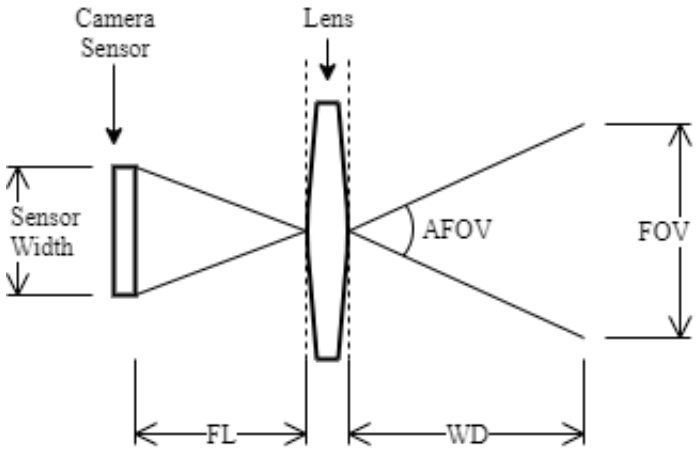

Figure 3.5: Ray Diagram for Simple Lens-Sensor System

$$FOV = 2 \times WD \times \tan \frac{AFOV}{2} \tag{3.1}$$

3.1.2 Categories of Experiments Conducted

Several experiments were conducted to characterize the materials and to identify the variables to be used in the experimental platform. These tests included the following:

1. Sessile drop tests to determine base plate surface energies of the exchangeable base plates;

2. Camera calibration tests to ensure accurate camera measurement techniques; and

3. Bubble formation and detachment experiments with different chamber design configurations and pumping parameters.

The methodologies for these experiments are discussed as follows and in further detail in Sections 3.2 and 3.3 with regards to the parameters tested in Phase 1 and Phase 2.

3.1.2.1 Sessile Drop Experiments

Sessile drop tests were performed on each of the base plate materials to experimentally determine their surface energies. First, each substrate was prepared by wiping the surface with an alcohol wipe and then rising with distilled water (H_2O) before allowing to air dry. Then, the substrate was placed on top of a mount on the optical table and leveled using a high-precision bubble level. Next, a high-speed camera was mounted on a positioning mount and leveled with the drop aligned in the FOV. The camera was adjusted vertically so that its central axis was at exactly the same height as the substrate. Then, a small drop of H_2O was pipetted onto each surface. After allowing 30 seconds to stabilize, the camera then captured the image of the drop. This procedure was repeated for the following substrates: Aluminum (Al), Teflon (PTFE), polycarbonate (PC), and quartz (SiO_2).

The surface energies for each substrate were calculated using Young's equation which relates the advancing contact angle to surface energy. The equation represents the balance of surface tension forces (or surface energy) at the solid-liquid-gas interface. Figure 3.6 shows the three forces: solid-gas surface tension, solid-liquid surface tension, and liquid-gas surface tension (γ_{sg}, γ_{sl}, and γ_{lg}, respectively). Young's equation assumes no other forces are acting on the bubble (Equation 3.2) [38][39]. Application of wetting theory has led to a number of methods of calculating surface energies. For example, the method derived from Young's Equation leads to Equation 3.3, where Φ (free energy ratio) is given by

Equation 3.4 [38]. V_s and V_l are the molar volume of the solid and the liquid respectively. For this research, operators measured contact angle θ from Sessile drop images and used Equations 3.3 and 3.4 to obtain surface energy values for each base plate. Contact angle can also be greatly influenced by surface roughness [40]. The effects of roughness were not studied in this thesis, but are included in the planned future work for this experimental research.

$$\gamma_{sg} = \gamma_{sl} + \gamma_{lg} \cos\theta \tag{3.2}$$

$$\cos\theta = 2\Phi(\frac{\gamma_{sg}}{\gamma_{lg}})^{1/2} - 1 \tag{3.3}$$

$$\Phi = \frac{4(V_s V_l)^{1/3}}{(V_s^{1/3} + V_l^{1/3})^2} \tag{3.4}$$

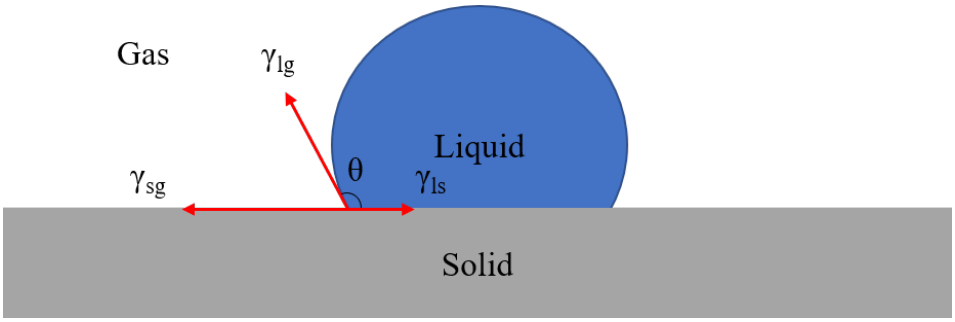

Figure 3.6: Surface Tension Forces at Sessile Drop Three-Phase Point

3.1.2.2 Camera Calibration Experiments

Imaging systems contain some measurable amount of distortion. Calibration tests are designed to measure this distortion so that it can be removed later. This process is necessary in order to produce accurate bubble volume measurements. The cameras for the experimental platform were calibrated using a 2D calibration method. The 2D calibration object used was a black and white checkerboard printed onto paper and taped to a flat

backing. The 2D calibration method used was first formulated by Zhang in 2000 [41], and was implemented using the OpenCV package in Python. Open CV is a computer vision package available in Python and C++. The function used, called calibrateCamera, utilizes a set of checkerboard images (shown in Figure 3.7) as an input and returns a matrix of distortion parameters for an imaging system. 1D, 3D, and contour-based calibration methods exist, but they are less robust and more computationally intensive [42][43]. New methods based on numerical analysis of probability distributions of calibration parameters also exist but are only a moderate improvement from the selected method [44].

Camera systems have two main types of distortion: intrinsic and extrinsic distortion [41]. Intrinsic distortion refers to the distortion that occurs inside of the lens-camera system and is modeled linearly as both radial and tangential distortions [28]. Extrinsic distortion is distortion that occurs outside of the lens-camera system and is also modeled linearly as both radial and tangential distortions. The method of camera calibration used is capable of determining linear distortions (intrinsic and extrinsic), however, nonlinear distortions cannot be accurately modeled. This calibrateCamera function employs a least-squares method for determining the approximated distortion parameters. A simple diagnostic was used by the operator to validate that the distortion parameters had been accurately determined: the reprojection error. The reprojection error (also returned from the calibrateCamera function) indicates the geometric error for projected point on an image and its measured point. The reprojection error is a good measure of calibration accuracy and should be as close to zero as possible. The goal of this experiment was to find a maximum acceptable reprojection error.

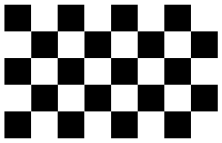

Figure 3.7: 2D Calibration Checkerboard

Undistorting the images captured by the imaging system is critically important for obtaining accurate measurements of real physical objects. To accurately measure the volume of a bubble, the system must be tuned in order to accurately undistort images. Furthermore, computer vision algorithms used determine bubble volume can only provide a volume of pixels; to obtain a physical measurement, a scale factor (SF) must also be obtained. The method used for obtaining a SF for the imaging system was capture images of an object with a precisely known size. Ball bearings of four sizes (0.125", 0.25", 0.5", and 0.75") were used for this task. After undistorting the images of the reference object, computer vision algorithms were used to calculate the pixel volume. The pixel volume was the divided by the known volume to obtain a scale factor for the imaging system. Once a SF for each ball bearing was obtained, the SFs were then averaged and the system was said to be fully calibrated. This procedure was repeated on a weekly basis to ensure that accurate measurements were being obtained.

3.1.2.3 Bubble Formation and Detachment Experiments

The third category of experiment conducted in this research project involved the formation and detachment of gaseous bubbles from a submerged plate with a small orifice in a liquid. In all cases the gas used was room air (estimated to be 78% N_2, 21% O_2, 0.9% Ar, and 0.04% CO_2) and the liquid used was distilled H_2O (Hill Country Fare brand). The bubble formation and separation experiment was conducted in Phase 1 and Phase 2. In Phase 1 the experiment utilized a single high-speed camera operating at 920 frames per second (FPS). In Phase 2 the experiment utilized both a two-axis high-speed camera system (X-axis and Y-axis) and a three-axis camera system where all cameras operated at 920 FPS. The procedures used to form and detach a bubble are outlined in Figure 3.8 and are detailed in Sections 3.2 and 3.3 with respect to the variables evaluated in Phase 1 and Phase 2.

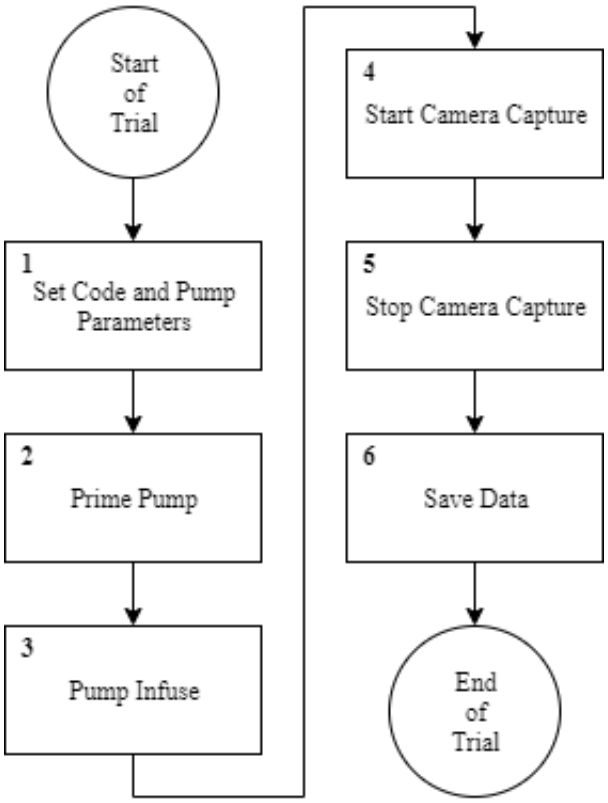

Figure 3.8: Experiment Procedures Flowchart

The first step in a bubble formation and detachment experimental trial (after calibration) was to set the appropriate pumping and wait time variables. These variables are: flow rate (FR), incremental pumped volume (IPV), and wait time (WT). Figure 3.9 shows the definitions of these terms graphically. These variables were set on the infusion pump and in the Python experiment control code. The next step was to prime the pump. This consisted of pumping a small amount of air through the pumping system. This step reduced the amount of time required to wait before a bubble formed and detached, and it also mitigated issues encountered with small, fractional microliter leaks in the pumping system. Step 3 executed the incremental pumping. In this step the operator executed a command in the Python code that started the timed triggering of the infusion pump in fractional microliter increments (the specified IPV).When the operator observed the bubble beginning to form at the orifice, the operator then executed the next step in the code:

triggering the cameras (either one, two, or all three) to capture at 920 FPS. The cameras continued to capture images at 920 FPS until the operator observed that the bubble detached from the orifice and executed the stop command in the Python code. The final step in the procedures occurred automatically in the code. Upon stopping camera acquisition, the code began saving the images from each camera sequentially. This was the final step in an experimental trial. Once the sequence was completed, it was be repeated as many times as necessary.

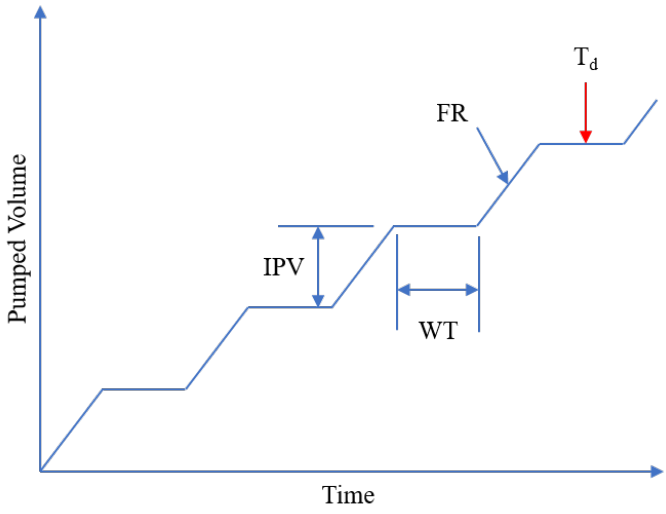

Figure 3.9: Illustration of Flow Rate (FR), Incremental Pumped Volume (IPV), Wait Time (WT), and Time of Bubble Detachment (T_d) as a Function of Pumped Volume and Time

The experiment naming convention applied in this thesis uses the following convention: P#-#.#, where the first number stands for the phase of the project, the second number stands for the test, and the third number stands for the variation of the test. Table 3.4 lists the Phase 1 and Phase 2 experiments by name and associated number.

Table 3.4: Bubble Formation and Detachment Experiment Names

Development Phase	Experiment Number	Experiment Name
Phase 1	P1-1.1	Preliminary Sensitivity Test
Phase 1	P1-1.2	Repeatability Analysis Experiment
Phase 2	P2-1.1	Flow Rate and Incremental Pump Volume Parametric Study
Phase 2	P2-2.1	Polycarbonate Incremental Pump Volume Sensitivity Test
Phase 2	P2-2.2	Multi-Plate Incremental Pump Volume Sensitivity Test

3.2 Phase 1 Methodology

In Phase 1 the main goal was to develop a proof of concept, validate components, and to generate an understanding of the most critical variables (sensitivity testing). The following section describes the experiment and variables that were investigated in Phase 1 of development including bubble formation experiments and imaging system tests.

3.2.1 Phase 1 Imaging System

The imaging system used in the Phase 1 experimental platform was a one-camera system. The one-axis camera system relied on axisymmetric assumptions to calculate volume measurements, and relied on manual measurements to obtain contact angles. The single camera was triggered at 920 FPS and with a resolution of 224 x 342 pixels (px). The reduction in pixels from the full resolution was justified by the fact that the camera was as close as possible to the fluid chamber, had no optical zoom, and the sides of the image contained no useful information. This reduction in resolution also had the benefit of allowing an increase from 860 FPS to 920 FPS with the same exposure time of 1 ms. This iteration of the imaging system was also put through the paces of camera calibration and used to determine an effective yet efficient calibration procedure. That calibration procedure is fully described in Section 3.1.2.2

3.2.2 Phase 1 Bubble Volume Measurement

In Phase 1, bubble volumes were measured in microliters using the infusion pump's displayed pumped volume (the total volume pumped since starting the experiment). The pumped volume was recorded from the infusion pump at time of detachment for a preceding bubble. When the next bubble formed, the pumped volume was recorded again. Lastly, pumped volume was recorded at time detachment for the second bubble. The bubble volume at detachment was then calculated by subtracting the pumped volume for the preceding bubble at detachment from the pumped volume for the final bubble at detachment.

3.2.3 Phase 1 Experiments

Two experiments were conducted in Phase 1: variable sensitivity tests and bubble volume tests. The preliminary sensitivity test, P1-1.1, varied the incremental pumped volume (IPV), the flow rate (FR), and the wait time between pumps (WT). This investigation was important for determining the range of operation for the experimental apparatus as well as the optimal parameters for forming bubbles. The repeatability analysis experiment, P1-1.2, used information from the preliminary sensitivity test to operated the apparatus at what was determined to be the optimal parameters for bubble formation, growth, and detachment. This variable configuration was conducted 22 times (n = 22) in order to determine the statistical repeatability of bubble volume measurements made by the instrument.

Table 3.5: P1-1.1 Experimental Parameters and Number of Trials

FR (µL/s)	IPV (µL)	WT (s)	Trials
10.0	10.0	1	1
10.0	2.0	1	1
1.0	0.5	1	1
1.0	0.25	1	1
1.0	0.25	2	1
0.5	0.1	2	1

Table 3.6: P1-1.2 Experimental Parameters and Number of Trials

FR (µL/s)	IPV (µL)	WT (s)	Trials
1.0	0.25	2	22

3.3 Phase 2 Methodology

In Phase 2 of the development of this experimental instrument, the main goal was to solve the issues observed in Phase 1 of development and to perform a more extensive evaluation of the system. This section describes the experiments and variables that were investigated in Phase 2 of development and testing, including bubble formation experiments and imaging system tests.

3.3.1 Phase 2 Imaging System

The Phase 2 imaging system consisted of both a two-camera imaging system and a three-camera imaging system. The two-camera system was used while image processing code was being developed for the three-camera system. Three cameras were always acquiring data in Phase 2 experiments, but the Z-axis camera data was not processed until later. The Phase 2 imaging system ran at the same exposure time (1 ms) and acquisition speed (920 FPS) as the Phase 1 system. The same resolution (224 x 342 px) was also maintained. The camera calibration procedures (discussed in Section 3.1.2.2) were updated for the Phase 2 imaging system.

Ultimately, the only major difference from the Phase 1 imaging system was the addition of Y-axis and Z-axis cameras. The X-axis, Y-axis, and Z-axis cameras were kept at mutually orthogonal angles. Levels and squares were used to ensure that each camera was in the correct orientation relative to the others and to the fluid chamber. Correct relative orientation is important for this system because of the 3D volume calculations that are used in the post processing code (discussed in Section 3.4.3).

3.3.2 Phase 2 Experiments

Three bubble formation and detachment experiments were conducted in Phase 2 (P2-1.1, P2-2.1, and P2-2.2). These experiments were conducted with two pumping parameters (IPV and FR) and three base plates. The first test, the flow rate and incremental pump volume parametric study (P2-1.1), was conducted with a PC base plate with a constant gas injection time (FR and IPV were both selected to inject air in 0.5 s intervals). The FRs and IPVs variables evaluated for this experiment are shown in Table 3.7. The next set of experiments, the polycarbonate incremental pump volume sensitivity test (P2-2.1), was conducted with a PC base plate, FR was held constant, and IPV was changed. The multi-plate incremental pump volume sensitivity test (P2-2.2) followed this same procedure (constant FR, dependent IPV) with aluminum, Teflon, and quartz base plates over a narrower range of IPVs ($0.20 - 1.00$ µL/s) than those in P2-2.1 ($0.2 - 7.50$ µL/s). The FR and IPV for these experiments are shown in Tables 3.8 and 3.9. Five trials were planned for all tests in Phase 2, however, in experiment P2-1.1, one configuration of variables was accidentally run six times and another four times (shown in Table 3.7).

Table 3.7: Experiment P2-1.1 Experimental Parameters and Number of Trials

base plate Material	**FR (µL/s)**	**IPV (µL)**	**Trials**
PC	0.5	0.25	5
PC	1.0	0.5	5
PC	1.5	0.75	5
PC	2.0	1.0	6
PC	2.5	1.25	5
PC	5.0	2.5	4
PC	10.0	5.0	5
PC	15.0	7.5	5

Table 3.8: Experiment P2-2.1 Experimental Parameters and Number of Trials

base plate Material	FR (µL/s)	IPV (µL)	Trials
PC	0.5	0.2	5
PC	0.5	0.25	5
PC	0.5	0.30	5
PC	0.5	0.40	5
PC	0.5	0.50	5
PC	0.5	0.75	5
PC	0.5	1.00	5
PC	0.5	1.25	5
PC	0.5	2.50	5
PC	0.5	5.00	5
PC	0.5	7.50	5

Table 3.9: Experiment P2-2.2 parameters

base plate Material	FR (µL/s)	IPV (µL)	Trials
PC, Al, PTFE	0.5	0.2	5
PC, Al, PTFE	0.5	0.25	5
PC, Al, PTFE	0.5	0.30	5
PC, Al, PTFE	0.5	0.40	5
PC, Al, PTFE	0.5	0.50	5
PC, Al, PTFE	0.5	0.75	5
PC, Al, PTFE	0.5	1.00	5

3.4 Image Analysis

The image analysis for this thesis project was conducted using code written in Python. The majority of the functions used for the complex computer vision algorithms were taken from the OpenCV library, where useful functions had already been developed and tested. The image analysis, also called post processing, was used primarily to determine bubble volume measurements. Images can be considered as a matrix of values ranging from 0 to 255, where 0 is black and 255 is white. Figure 3.10 illustrates this concept. The computer vision analyses implemented in Python manipulate these image matrices to measure bubble volumes.

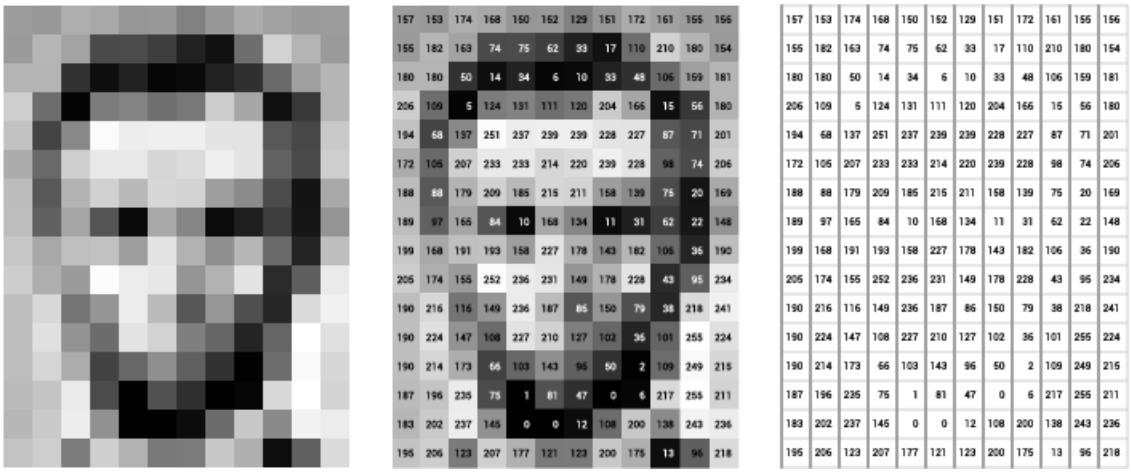

Figure 3.10: Image Matrix of Pixel Values. Reprinted from Stanford Artificial Intelligence Laboratory, 2015 [45]

Two methods of the bubble volume analysis were pursued: axisymmetric analysis and three-camera analysis. While significantly different in their approach, both of these methods relied on the same initial post processing step called "masking".

3.4.1 Bubble Image Masking

The steps for masking a bubble image are described as follows. The masking algorithm is applied to every bubble image before volume or contact angle measurements are conducted. Figure 3.11 shows the initial steps for post processing.

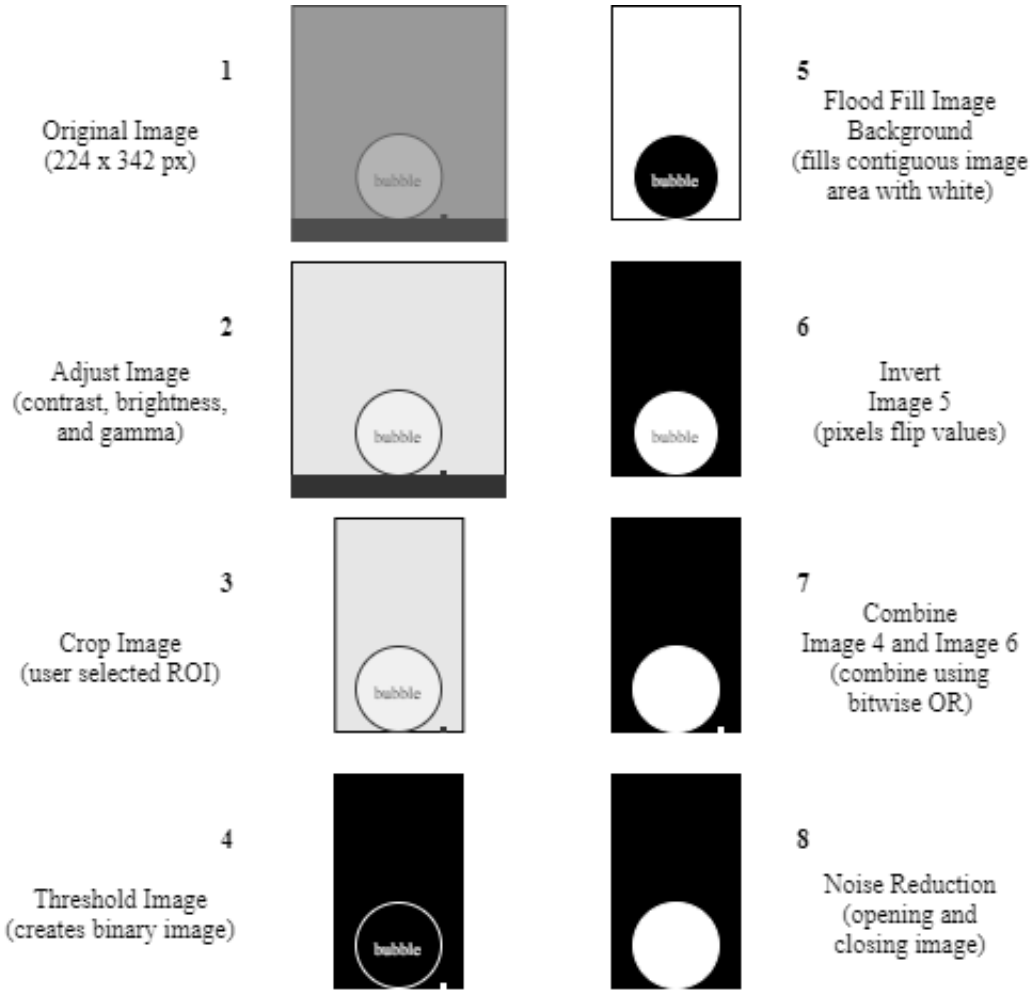

Figure 3.11: OpenCV Image Processing Steps

Image analysis begins with an original bubble image that was acquired during and experimental trial. This image can have a variety of defects that make it difficult for the computer vision algorithms to process. The first step was to improve image clarity; this was a trial and error process where the operator adjusted the image contrast, brightness, and gamma. Contrast and brightness adjust the image according to Equation 3.5, where $\boldsymbol{f(i,j)}$ is an input image pixel values, α is the contrast, β is the brightness, and $\boldsymbol{g(i,j)}$ is the output image pixel values. Gamma correction adjusts the image according to Equation 3.6, where I is an input image, γ is the gamma value, and O is the output image

(before scaling back down to values between 0 and 255). These parameters were finely tuned until the image has as much clarity as possible. An example of an adjusted image can be seen in Figure 3.12. Next, the adjusted image was cropped by the operator who selects a region of interest (ROI) around the bubble. This step helped eliminate unwanted features such as the base plate. The ROI was selected to: completely eliminate the base plate, center the bubble, cut off unneeded edges. The next five steps (4-8) were critical for creating a masked bubble image. Step 4 converted the standard [0-255] image into a purely black and white image [0, 255], where 0 and 255 were the only pixel values. This was accomplished by using the OpenCV threshold command which sets all pixels below and above a threshold to 0 and 255 respectively. Step 5 filled the contiguous background area in the image with white pixels leaving only the bubble interior. Step 6 inverted the image by flipping black pixels to white and white pixels to black. In Step 7, images formed in Step 4 and Step 6 were combined using the bitwise OR function in OpenCV. Bitwise OR in OpenCV compares pixels in two images (A and B) and sets an output pixel to white if that pixel is white in either A or B, otherwise the output pixel is set to black. The final step was to perform some noise reduction by calling the OpenCV opening and closing functions on the image in Step 7. The final image produced in Step 8 is denoted as the "masked bubble image" and was used in the following bubble volume calculation analyses. An example masked bubble image is also shown in Figure 3.12

$$\boldsymbol{g(i,j)} = \alpha \boldsymbol{f(i,j)} + \beta \tag{3.5}$$

$$O = (\frac{I}{255})^{\gamma} \times 255 \tag{3.6}$$

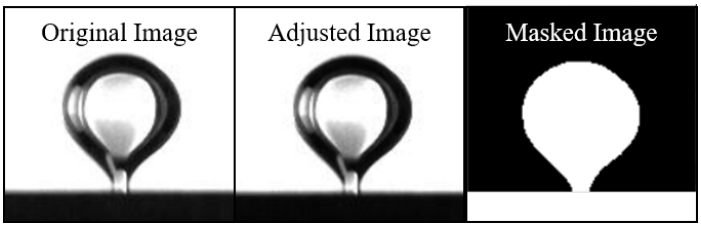

Figure 3.12: An Example of Masked Bubble Image Processing of a Bubble Image Captured in Experiment P2-2.2

3.4.2 Axisymmetric Volume Measurement Methodology

Two methods were developed for the axisymmetric analysis of bubble volume. The first method utilized a masked bubble image from a single camera. The bubble in the masked image was analyzed using the equivalent spherical diameter (ESD) function. These two steps are shown in Figure 3.13. The second method of axisymmetric bubble volume calculation used the exact same procedure with the addition of a second orthogonal image. The calculated volumes from each image were then compared.

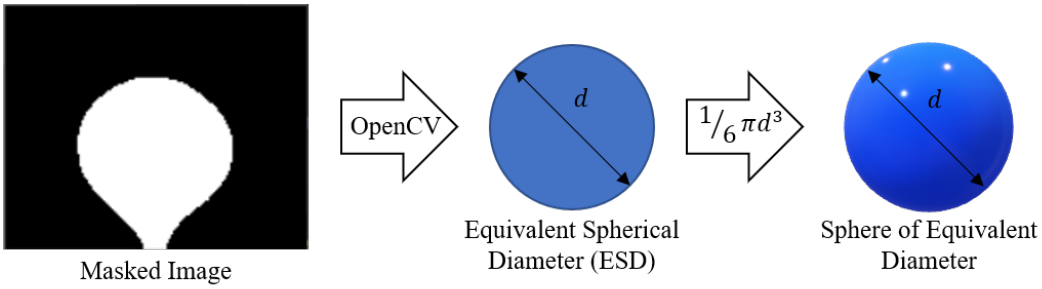

Figure 3.13: Bubble Volume Calculation Using Axisymmetric Assumption

3.4.3 Three-Camera Volume Measurement Methodology

The three-camera analysis used images from an X-axis camera, a Y-axis camera, and a Z-axis camera. Information was extracted from the three orthogonal masked bubble

images. Figure 3.14 shows the general steps used for generating a bubble volume measurement using three orthogonal images. A critical consideration was that a single pixel in each image does not have the same length in the real world. For this reason, sub-pixel slices of 0.001 of an inch were used for the following steps. Diameters Φ_x and Φ_y were measured across the bubble in the X-axis and Y-axis images at each 0.001" cross section. The Z-axis image was then scaled to match it's diameter along both axes for each 0.001" cross section. Then, the area of each cross-sectional Z-axis image was measured with OpenCV and multiplied by a thickness of 0.001". Adding up all of these disks calculated the total volume of the bubble measured by three cameras.

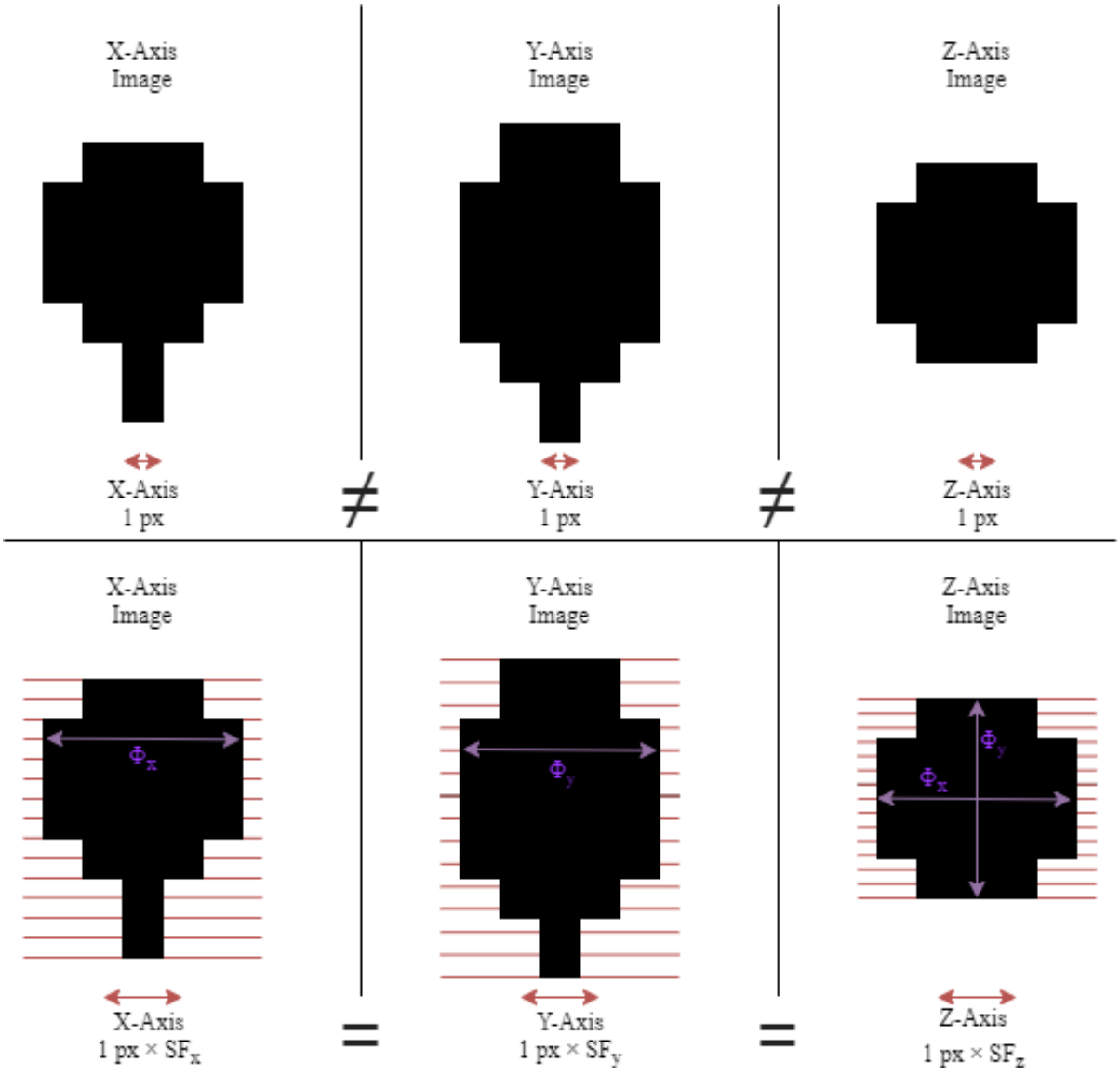

Figure 3.14: Bubble Volume Calculation Using Three-Camera Analysis

While the three-camera method showed promise, insufficient lighting prevented the Z-axis camera from capturing the bubble shape (discussed further in Section 5.4.3). Instead of using the Z-axis image, an elliptical cross section was assumed and the rest of the three-camera analysis was implemented as described above. This method can be easily converted back to using the Z-axis masked bubble images if proper lighting is achieved

in the future.

3.4.4 Contact Angle Measurement Methodology

The bubble contact angle analysis was conducted using the same methodology in Phase 1 and Phase 2. This analysis utilized a masked image of a bubble one frame before detachment. For this analysis, it was assumed that the bottom plate was perfectly level. The right and left contact angles were measured using manual methods and averaged for every bubble. The manual methods used included printed images with a pen and protractor, and through OpenCV methods where a line was manually drawn. Figure 3.15 shows the two contact angles on a masked bubble image. These angles (θ'_{Left} and θ'_{Right}) are not measured directly on the point of connection to the orifice, but rather the point where the bubble shape begins to take definition. While this method is prone to human error, it has been used by other investigators in the past [16].

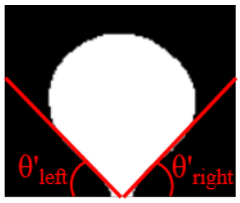

Figure 3.15: Left and Right Contact Angles on a Bubble During Detachment

4.1 Final Design Configuration

The final design configurations for Phase 1 and Phase 2 are provided in this section. The specific hardware that was purchased or designed to create the experimental apparatus is also discussed. The Phase 1 configuration was designed to meet less strict requirements than Phase 2 and was designed to be used as a proof of concept. The Phase 2 configuration was designed to meet all requirements in Table 3.1. Figure 4.1 shows the final design configuration for Phase 2.

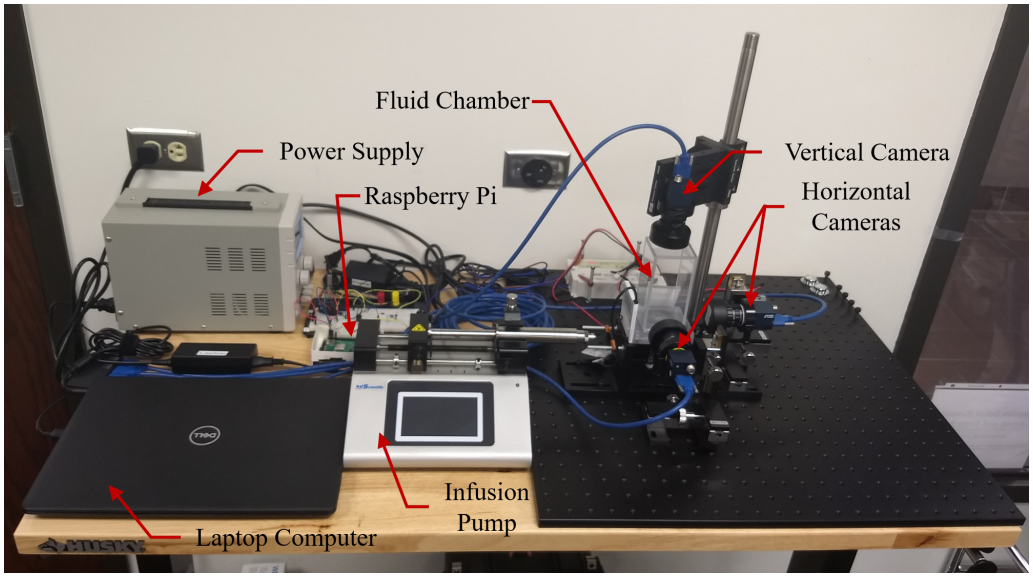

Figure 4.1: Phase 2 Experimental Platform with Components Labeled

4.1.1 Phase 1 Experimental Platform Configuration

The Phase 1 experimental platform was designed with three major systems, outlined in Section 3.1.1. This design was a proof of concept and was not required to meet all requirements. Specifically, this design was designed to use one camera and not the mini-

mum of two cameras that is listed in requirement R9 (Table 3.1).

4.1.1.1 Phase 1 Passive Components

The selected lab bench was 24″ x 46″ and acted as a workstation for all of the experiment platform and computing components. The breadboard optical table (24″ x 24″) covered half of the workbench and was a solid aluminum block with M6 tapped holes. The lab bench and optical breadboard did not have vibration isolation systems.

The two mounts used in the Phase 1 experiment platform, shown in Figure 4.2, included a 3D printed fluid chamber mount and a 3D printed camera mount. These components were fixed to the optical table using optical table clamps to prevent unwanted movement of the mounted components.

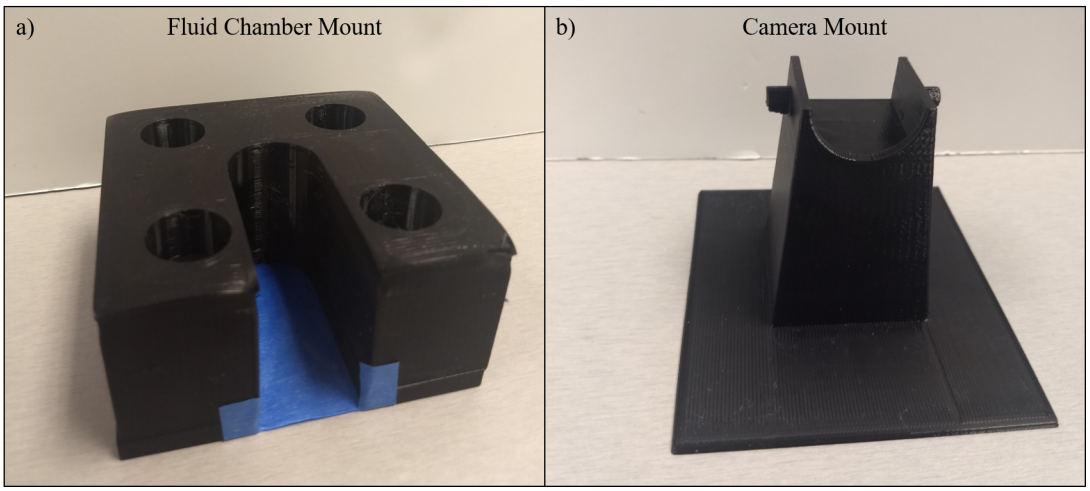

Figure 4.2: (a) Phase 1 Fluid Chamber Mount and (b) Phase 1 High-Speed Camera Mount, Made from 3D Printed Material

The Phase 1 fluid chamber is shown in Figure 4.3. The Phase 1 fluid chamber was made from extruded PC and two PC sheets for the top and bottom plates. The walls were made from a square 2″ x 2″ extruded PC tube that was 2.4″ tall and 1/8″ thick. The top and bottom sheets were also 1/8″ thickness. The bottom sheet had a small orifice drilled

into the PC for the injection of air by the pumping system. The top plate had a larger hole drilled in the center to allow for pumped air to escape the fluid chamber. Two rubber gaskets were fitted between the chamber walls and top and bottom plates. These gaskets were clamped on all four corners of the top and bottom plates allowing the vessel to be sealed.

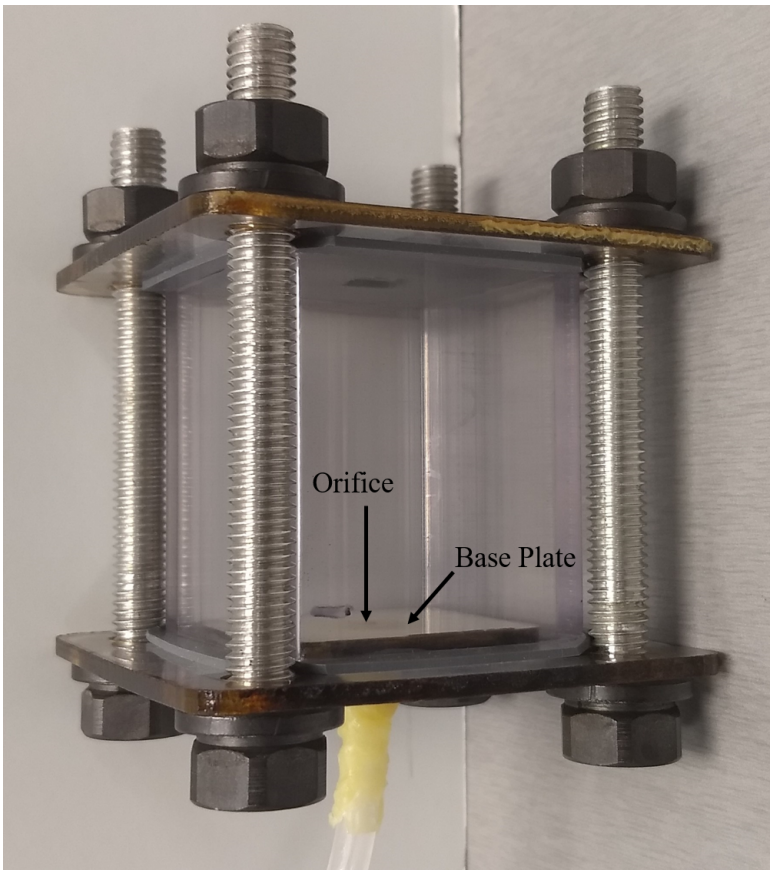

Figure 4.3: Phase 1 Fluid Chamber

4.1.1.2 Phase 1 Pumping System

The pumping system in Phase 1 utilized a LEGATO 110 infusion pump with a 20 mL gastight syringe from Harvard Apparatus (shown in Figure 4.4). The syringe was connected to the fluid chamber orifice through a series of pipes, valves, and fittings. The

gastight syringe was connected to 1/8″ ID Tygon tubing with a luer lock to barbed connector fitting. The Tygon tube then connected to a three-way normally closed solenoid valve. The solenoid connections were 10-32 UNF to barbed connectors. The tubing out of the solenoid valve was connected directly to the bottom plate of the fluid chamber. Epoxy and rubberized adhesive were used to attach to Tygon tube to an inlet slot on the bottom of the bottom plate. The base plate used in the Phase 1 experiment was made from 1/8″ PC sheet and had a diameter of 1.6 mm.

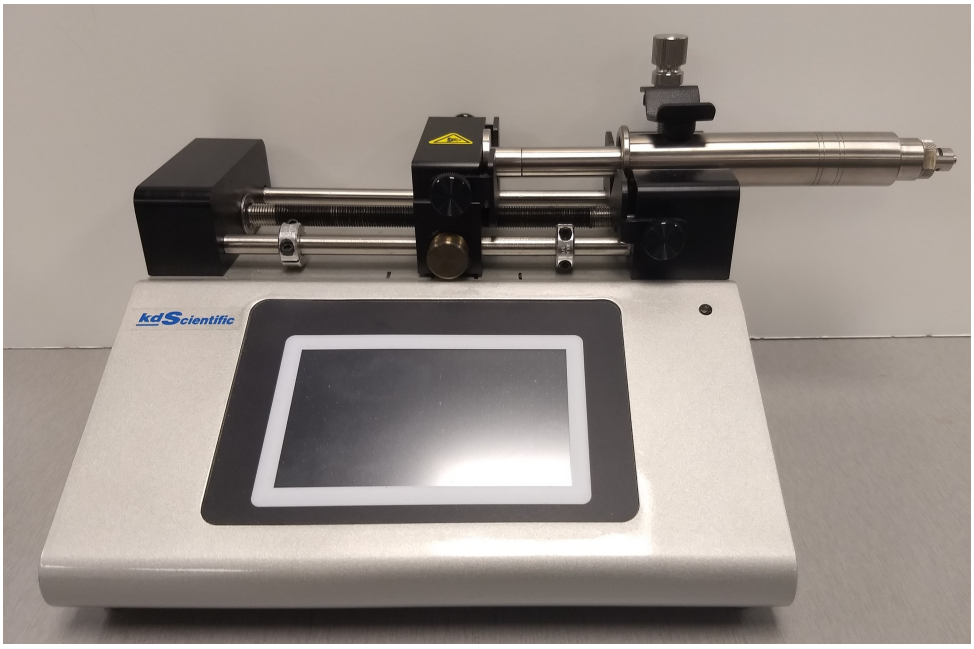

Figure 4.4: LEGATO 110 Series Infusion Pump with 20 mL Gastight Syringe

The pumping system was controlled by a Dell laptop computer and Raspberry Pi 3 B+. The laptop and Raspberry Pi operated in a master/slave configuration where the laptop commanded the Raspberry Pi to execute specific functions. The master/slave communication was executed on the laptop using Python code developed in the AHSL. The Raspberry Pi was needed to interface with the infusion pump and the solenoid valve. The Raspberry Pi sent commands from the laptop to the infusion pump through an RS-232 in-

terface using the GPIO pins on the Raspberry Pi. The Raspberry Pi's interface with the solenoid valve also used the digital GPIO output. The 3.3 V digital I/O signal output from the Raspberry Pi was used to switch the solenoid valve off and on. A switching circuit for the solenoid valve was designed and is shown in Figure 4.5. The solenoid was powered by a DC power supply and switched using an NPN transistor. The other components in this circuit were a resistor and a flyback diode.

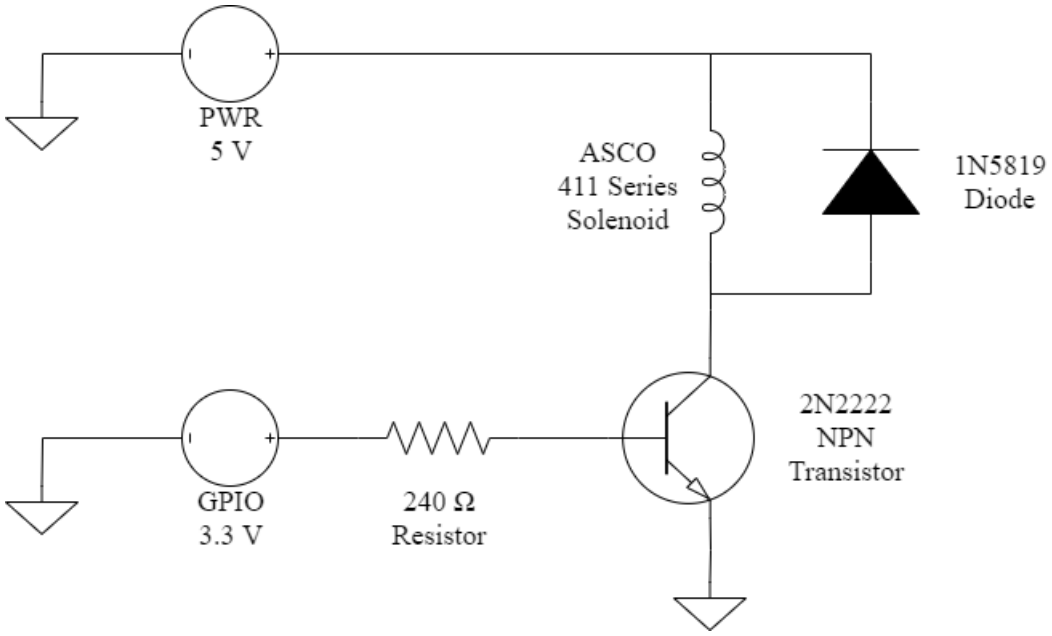

Figure 4.5: Solenoid Circuit

4.1.1.3 Phase 1 Imaging System

The high-speed camera used in Phase 1 was a CMOS global shutter camera made by Daheng Imaging. The model used was a monochrome MER-031-860U3M camera with a 1/4″ sensor format. The camera was capable of continuous image acquisition up to 860 FPS with full resolution at 640 x 480 px. Figure 4.6 shows this camera in the 3D printed positioning mount that was used in Phase 1. The camera axis was arranged to be normal to one of the fluid chamber walls. The camera system was triggered with an exposure

time of 1 ms with the image cropped to increase speed. The image was cropped to 224 x 342 px, which led to an acquisition speed of 920 FPS. The lens used with the high-speed camera was a 3.5 mm fixed focal length lens with low distortion. This lens had an adjustable aperture from f/2 to f/11 and a working distance of 0 mm to ∞ mm. The light used for Phase 1 was a 6 cm x 6 cm LED panel from LEDCONN. The frequency of this LED panel was sufficiently high that the cameras did not pick up a variation in light intensity. The LED panel was placed opposite of the camera to backlight the fluid chamber.

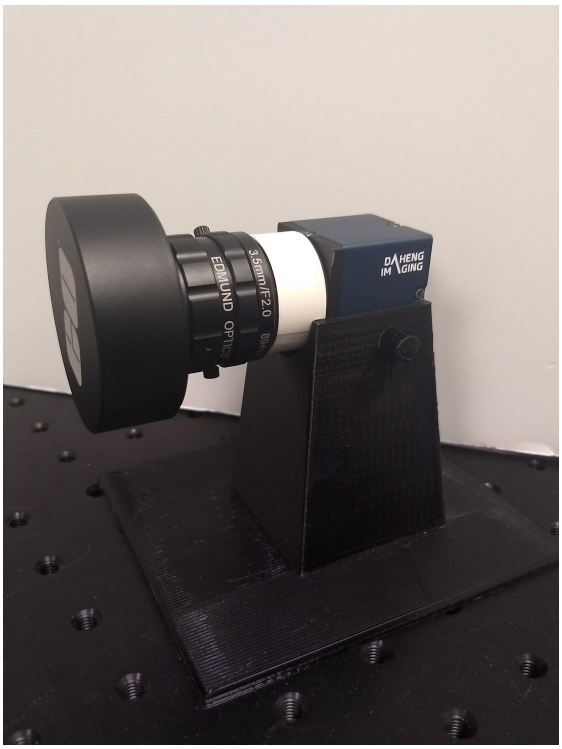

Figure 4.6: Daheng Imaging MER-031-860U3M Camera on 3D Printed Camera Mount

4.1.2 Phase 2 Experimental Platform Configuration

The final configuration that was designed for Phase 2 of this design project is detailed in this section. The Phase 2 experimental platform is shown in Figure 4.1. The design and

selected components of each systems is provided in the following subsections.

4.1.2.1 Phase 2 Passive Components

The Phase 2 fluid chamber was designed to meet the requirements discussed in Section 3.1.1. The Phase 2 fluid chamber was constructed from PC sheets and machined PC blocks that were glued together. The fluid chamber walls were 4.5″ tall 1/8″ thick. The top plate was also 1/8″ thick and had a small hole drilled into the corner to allow pumped air to escape. The lower portion of the chamber was made from a machined block of PC with a flange and O-ring channel for fixing and sealing a bottom plate. The O-ring channel was designed for a 1/16″, fractional width O-ring. The bottom plates for the Phase 2 fluid chamber were designed to be easily removable so that different base plate materials could be tested. The bottom plate was also made from machined PC block and was sealed to the fluid chamber flange with screws and an O-ring. The base plates are discussed further in the Section 4.1.2.2.

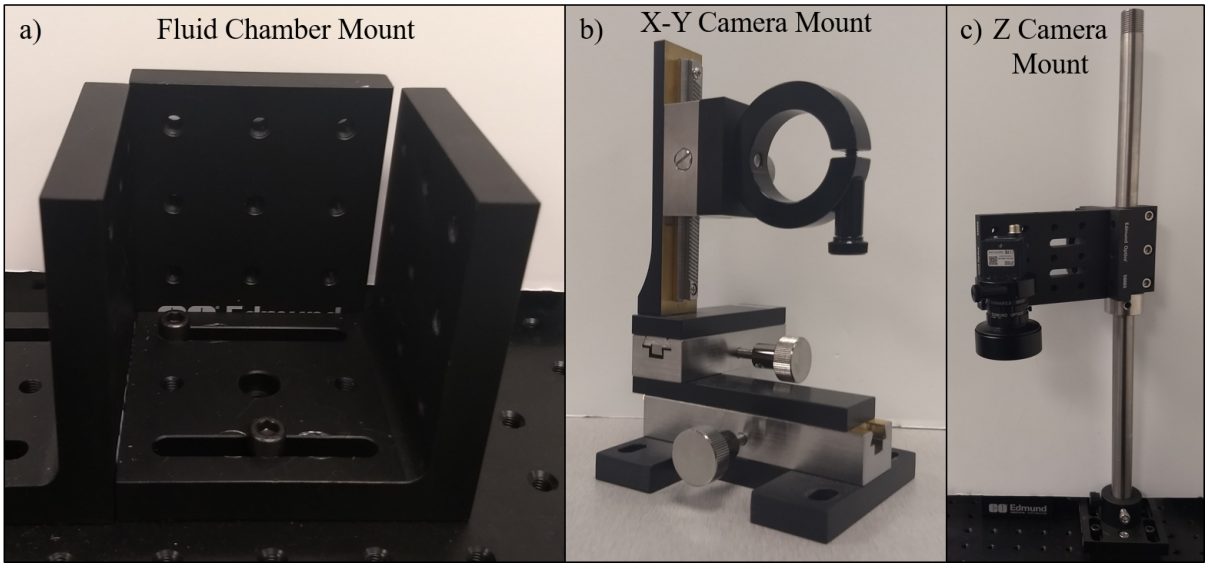

Figure 4.7: (a) Phase 2 Fluid Chamber Mount, (b) X-Y Camera Mount, and (c) Z-Camera Mount

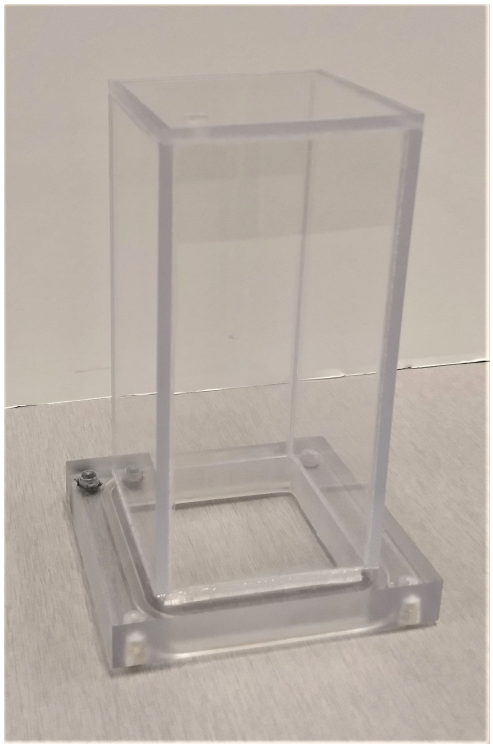

Figure 4.8: Phase 2 Fluid Chamber

4.1.2.2 Phase 2 Pumping System

The Phase 2 experimental platform used the same many of the same pumping system components that were used in Phase 2, with the addition of a greater selection of bottom plates and base plates. Both phases utilized a LEGATO 110 infusion pump with a 20 mL gastight syringe from Harvard Apparatus (shown in Figure 4.4). The syringe was connected to the fluid chamber orifice through a series of pipes, valves, and fittings. The gastight syringe was connected to 1/8" ID Tygon tubing with a luer lock to barbed connector fitting. The Tygon tube then connected to a three-way normally closed solenoid valve. The solenoid connections were10-32 UNF to barbed connectors. The tubing out of the solenoid valve was connected directly to the bottom plate of the fluid chamber. Epoxy and rubberized adhesive were used to attach to Tygon tube to an inlet slot on the bottom of the bottom plate.

The design of a removable bottom plate in Phase 2 allowed for the exchange of materials of different surface energies. The three base plates used in Phase 2 (shown in Figure 4.9) are made from Al, PTFE, and PC, with plans to add a fourth: SiO_2. The orifice diameter for the Phase 2 base plates was reduced to 0.8 mm. The details of each of these plates is provided in Table 4.1.

Table 4.1: Phase 2 Base Plate Parameters

Base Plate Material	**Thickness (inches)**	**Surface Finish**
Aluminum (Al)	0.25	Specular #8 reflective finish
Teflon (PTFE)	0.75	Machined finish
Polycarbonate (PC)	0.125	Smooth factory finish
Quartz (SiO_2)	0.25	Smooth factory finish

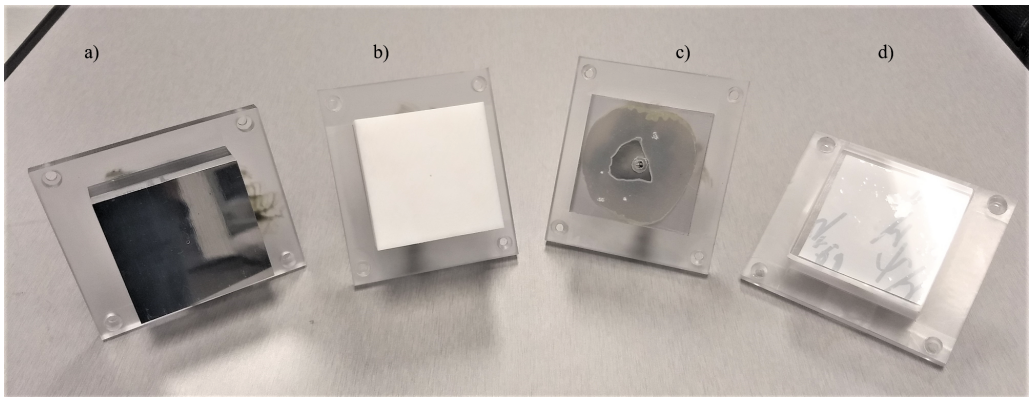

Figure 4.9: Phase 2 Base Plates: Aluminum (a), Teflon (b), Polycarbonate (c), Quartz (d)

4.1.2.3 Phase 2 Imaging System

The three high-speed cameras used in Phase 2 were the same MER-0310860U3M camera made by Daheng Imaging that was used in Phase 1. Figure 4.10 shows this camera in the X-Y-Z positioning mount that was used in Phase 2. The three cameras were arranged

in mutually orthogonal axes (X-axis, Y-axis, and Z-axis) that were aligned with the fluid chamber walls and top. The cameras were triggered with an exposure time of 1 ms. The images were cropped to 224 x 342 px, which led to an acquisition speed of 920 FPS. The lenses used with the high-speed cameras were the same 3.5 mm fixed focal length lens used in Phase 1. This lens had an adjustable aperture from f/2 to f/11 and a working distance of 0 mm to ∞ mm. The lights used for Phase 2 were two 6 cm x 6 cm LED panel from LEDCONN (the same model that was used in Phase 1). The two LED panels were arranged to backlight the fluid chamber from the X-axis and Y-axis perspectives.

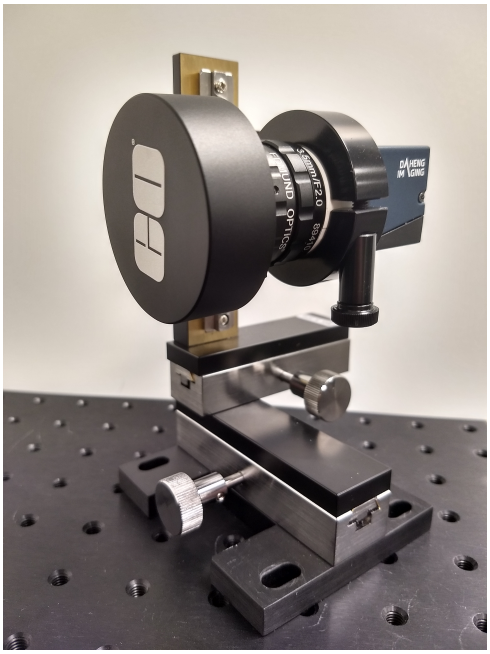

Figure 4.10: Daheng Imaging MER-031-860U3M Camera on X-Y-Z Positioning Mount

This concludes the overview of the final design configurations for the Phase 1 and Phase 2 experimental platforms. Sections 4.2−4.5 report the results from various experiments conducted using the Phase 1 and Phase 2 experimental platforms.

4.2 Sessile Drop Test Results

The Sessile drop test results are shown in Figure 4.11 and Table 4.2. The advancing Sessile drop contact angles (left and right) were measured and averaged across five trials for each surface. During this experiment, the room air and distilled water temperatures were 24.8 °C and 25.9 °C, respectively. Next, Equation 3.3 was used to calculate the solid-gas surface energy of each surface. Lastly, the results were tabulated and compared to published data in Table 4.2. SiO_2 had the highest surface energy at 50.4±5.5 mJ/m^2, and PTFE had the lowest surface energy at 11.3±1.3 mJ/m^2.

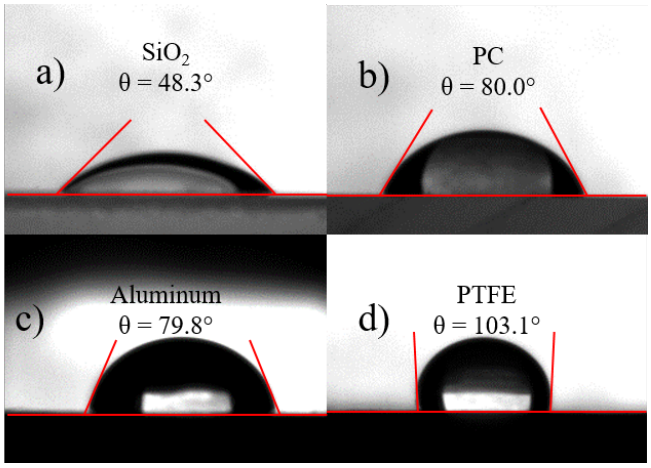

Figure 4.11: Measured Sessile Drop Advancing Contact Angle Results for SiO_2 (a), PC (b), Al (c), and PTFE (d) Base Plates (n = 5)

Table 4.2: Sessile Drop Test Results (n = 5) and Comparable Published Results

Surface Material	**Measured Sessile Drop Contact Angle**	**Calculated Surface Energy (mJ/m^2)**	**Published Surface Energy (mJ/m^2)**
SiO_2	48.3±6.9°	50.4∓5.5	30 – 76 [46]
PC	80.0 ±2.7°	34.4∓2.7	34 – 50 [47]
Al	79.8 ±3.7°	25.4∓2.8	33 – 45 [48][49]
PTFE	103.1 ±2.6°	11.3∓1.3	14 – 26 [50]

4.3 Camera Calibration Test Results

The camera calibration tests were conducted to determine the distortion parameters of the system (intrinsic and extrinsic to the lens-camera system), and to determine the SF for each camera. The first portion of the test allows distortions to be removed in future image analyses and the second portion allows real, physical distance and volume measurements to be obtained from pixel measurements. An example of the output parameters from a calibration conducted on January 6th, 2020 is shown in Table 4.3. These results were analyzed by examining the reprojection error which was used as a heuristic to determine the goodness of calibration. Calibrations were accepted if the reprojection error was below 0.220. The SF was calculated through the method outlined in Section 3.1.2.2 for each of the four ball bearings (0.125", 0.250", 0.500", and 0.750" diameter). It is important to note that the reported SF is the average of these four measurements made using the computer vision calibration algorithm. The standard deviation is also reported for this analysis. The average percent error (PE) was calculated from the SFs and their standard deviations using Equation 4.1. The PE was found to be 3.52%.

Table 4.3: Example of Camera Calibration Results from January 6th, 2020

Camera	**Reprojection Error**	**Mean Scale Factor (in/px)**	**Standard Deviation of Scale Factor (in/px)**
X-axis	0.169	1.91×10^{-3}	6.45×10^{-5}
Y-axis	0.198	2.16×10^{-3}	6.94×10^{-5}
Z-axis	0.150	4.04×10^{-3}	2.58×10^{-4}

$$PE = \overline{\left(\frac{\sigma_{SF}}{\mu_{SF}}\right)} \times 100\% \tag{4.1}$$

Figure 4.12 shows a distorted and undistorted ball bearing image side-by-side. From

these images it appears as if only minor distortions are present in the system. These images provided an additional check that no anomalies occurred during calibrations.

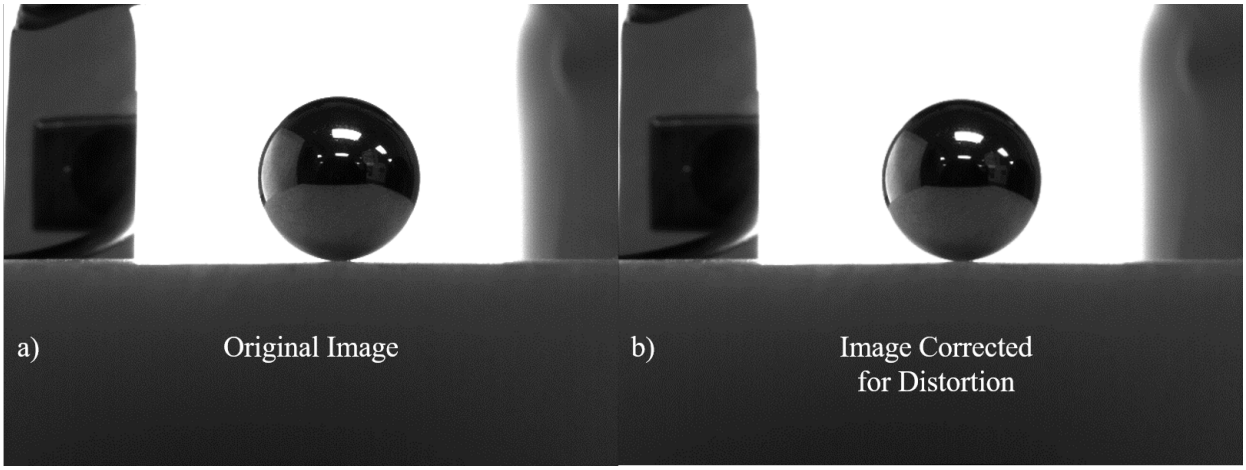

Figure 4.12: (a) Original Image of Calibration Ball Bearing (0.5″ Diameter) and (b) Image of Calibration Ball Bearing Corrected for Distortion, No Visible Differences

4.4 Experiment Phase 1 Results

The results from the two experiments conducted in Phase 1 are presented in the following sections. The experiments in Phase 1 examined variations in FR, IPV, and WT as well as bubble volume at detachment and contact angle at detachment. The bubble volumes in Phase 1 were calculated using the method outlined in Section 3.2.2.

4.4.1 P1-1.1 Preliminary Sensitivity Test Results

The preliminary sensitivity test (P1-1.1) was conducted over one day and used one camera calibration. The fluid used was distilled water and the gas was room air. A PC base plate was used for this experiment. This experiment was a qualitative analysis on the effects of instrument parameter (FR, IPV, and WT). These parameters were adjusted to a variety of levels which are reported in Table 3.5 and are reposted in Table 4.4 along with recorded observations.

Table 4.4: P1-1.1 Experimental Parameters and Observations

FR (µL/s)	IPV (µL)	WT (s)	Trials	Observations
10.0	10.0	1	1	Bubbles detached during single IPV periods
10.0	2.0	1	1	Bubbles detached during single IPV periods
1.0	0.5	1	1	Bubbles detached after $3-5$ IPV periods and some detached during IPV periods
1.0	0.25	1	1	Bubbles detached after 14 IPV periods and some detached during IPV periods
1.0	0.1	2	1	No bubble formation or detachment
0.5	0.25	2	1	Bubbles detached after 14 IPV periods and all detached during a wait time

4.4.2 P1-1.2 Repeatability Analysis Experiment Results

The repeatability analysis experiment (P1-1.2) was conducted over three days and used a single camera calibration. The fluid used was distilled water with a temperature ranging from 25.8 °C to 26.9 °C. The gas used was air with a temperature ranging from 24.4 °C to 25.1 °C. A PC base plate was used for this experiment. No parameters were varied during this test: FR, IPV, and WT were kept at the values listed in Table 3.6. A total of 22 trials were conducted to determine the precision of the experimental apparatus.

4.4.2.1 Experiment P1-1.2 Volume Data Analysis

The bubble volume was recorded in this experiment using the method outlined in Section 3.2.2. These volumes are plotted in Figure 4.13. The average bubble volume at detachment across 22 trials was 30.4±3.9 µL. This corresponds to a PE of 12.7%. These results were not able to be compared with computer vision volume analyses because of a lack of clarity in the Phase 1 fluid chamber.

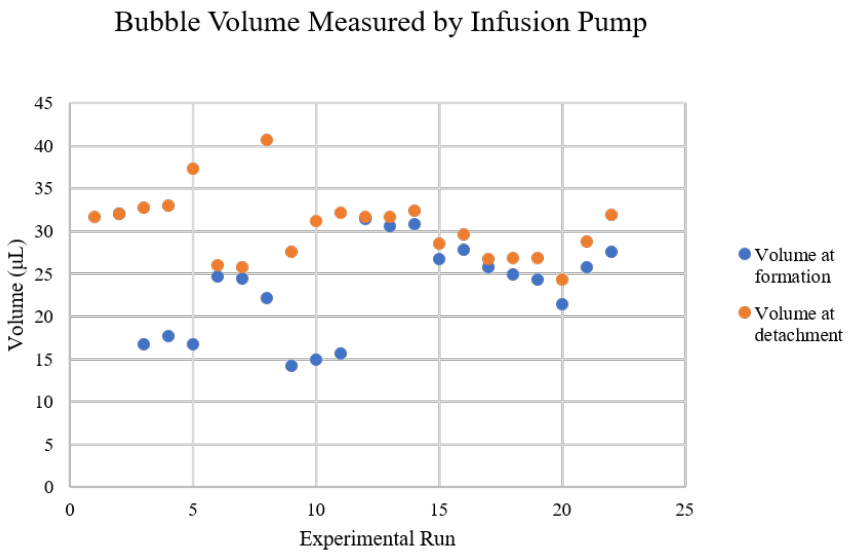

Figure 4.13: P1-1.2 Bubble Volumes at Formation and Detachment on PC Base Plate (22 Experimental Trials, Room Air in Distilled Water)

4.4.2.2 Experiment P1-1.2 Contact Angle Data Analysis

The bubble contact angles at detachment for this experiment are plotted in Figure 4.14, below. The left and the right contact angles for each bubble were recorded and then averaged. The average bubble contact angle at detachment was 55.1±5.3°. The average left contact angle was 54.1±5.4°, and the average right contact angle was 56.0±6.0°.

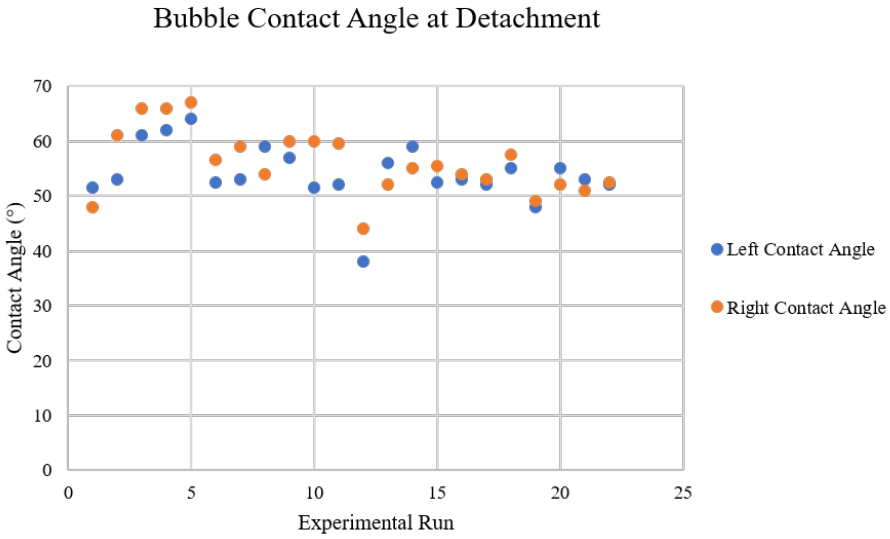

Figure 4.14: P1-1.2 Bubble Contact Angles at Detachment on PC Base Plate (22 Experimental Trials, Room Air in Distilled Water)

4.4.2.3 Experiment P1-1.2 Comparison to Initial CFD Model

The experimental results from the repeatability analysis experiment (P1-1.2) were compared to an initial CFD model. The model was developed in OpenFOAM by doctoral student Paul Burke and AHSL director Dr. Bonnie Dunbar. Figure 4.15 shows a time-lapse of bubble detachment in 1 g in the experimental instrument and Figure 4.16 shows a time-lapse of bubble detachment in the CFD model under the same parameters. The average bubble volume and contact angles are compared in Table 4.5. The validation of CFD models is outside the scope of this project but is a part of the future work for this research. This initial comparison was included for completeness.

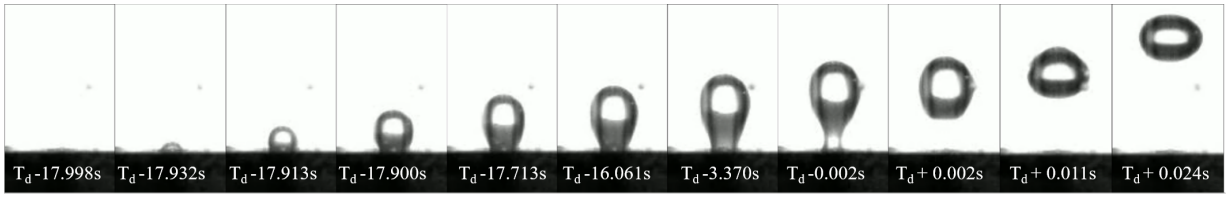

Figure 4.15: Experiment P1-1.2 Bubble Detachment Time-Lapse with Detachment Time (T_d) Labeled

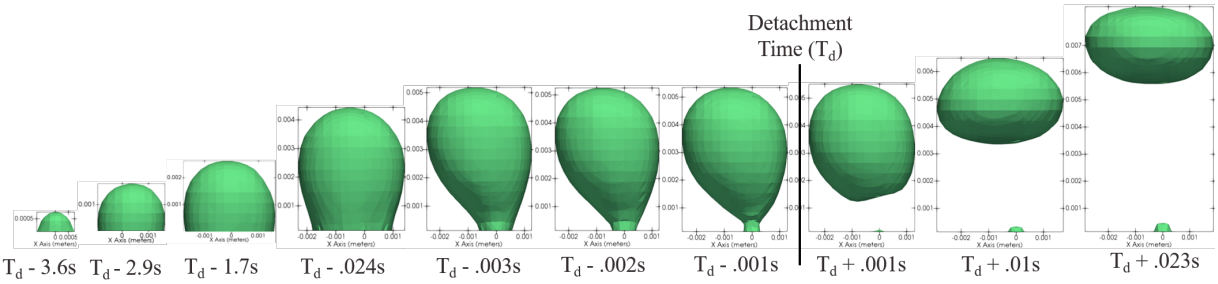

Figure 4.16: CFD Bubble Detachment Time-Lapse with Detachment Time (T_d) Labeled (Courtesy of PhD Candidate Paul Burke)

Table 4.5: P1-1.2 Experimental and CFD Results

Method	**Volume at Detachment (µL)**	**Contact Angle at Detachment (°)**
Experimental Results	30.4±3.9	55.1±5.3
CFD Results	33.02±0.25	52

4.5 Experiment Phase 2 Results

The results from the three experiments conducted in Phase 2 are presented in the following sections. Each experiment in Phase 2 examined bubble volume at detachment and contact angle at detachment. The bubble volumes in each experiment were calculated using the two computer vision methods outlined in Section 3.4.2 and Section 3.4.3.

4.5.1 P2-1.1 Flow Rate and Incremental Pump Volume Parametric Study Results

The flow rate and incremental pump volume parametric study (experiment P2-1.1) was conducted over four days and two separate camera calibrations. The fluid used was distilled water with a temperature ranging from 23.8 °C to 25.2 °C. The gas used was air with a temperature ranging from 22.4 °C to 23.6 °C. A PC base plate was used for this experiment. The parameters that were varied were FR and IPV and are shown in Table 3.7. FR and IPV were changed such that the gas injection time was always 0.5 seconds (the FR was always twice the IPV).

4.5.1.1 P2-1.1 Flow Rate and Incremental Pump Volume Parametric Study Volume Data Analysis

The bubble volume in the flow rate and incremental pump volume parametric study (experiment P2-1.1) was obtained using an axisymmetric analysis (Section 3.4.2) and a three-camera analysis (Section 3.4.3). The results from the axisymmetric analysis are shown in Figure 4.17 and Figure 4.18, below. These graphs show the bubble volume calculated through the axisymmetric analysis plotted against FR and IPV. Since these two variables were scaled proportionally, there is no difference in where the points are plotted on each graph: only the scales differ. These graphs show that the bubble volume was increasing at low FRs and IPVs and then began decreasing as FR and IPV continued increasing. This transition occurred at 2.5 µL/s FR and 1.25 µL IPV. The data point at the lowest FR and IPV (0.5 µL/s and 0.25 µL, respectively) was the only data point that does not follow this general trend. More trials at these parameters and other close FRs and IPVs would be required to determine whether this was an outlier or an accurate measurement. The smallest bubble volume measured (at FR = 1.0 µL/s) was 7.31±0.83 µL and the largest bubble volume measured (at FR = 0.5 µL/s) was 22.92±0.65 µL. The Y-axis volume measurements were, on average, 1.46±1.90 µL smaller than the X-axis volume measurements.

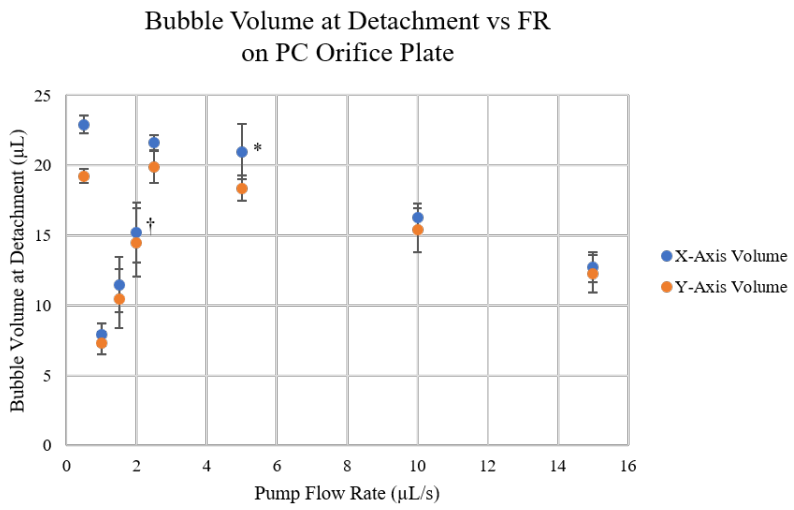

Figure 4.17: P2-1.1 Axisymmetric Bubble Volume at Detachment for X and Y Axes vs Flow Rate (FR) on a PC Base Plate (Five Experimental Trials Except Where Marked by * or †, Room Air in Distilled Water)

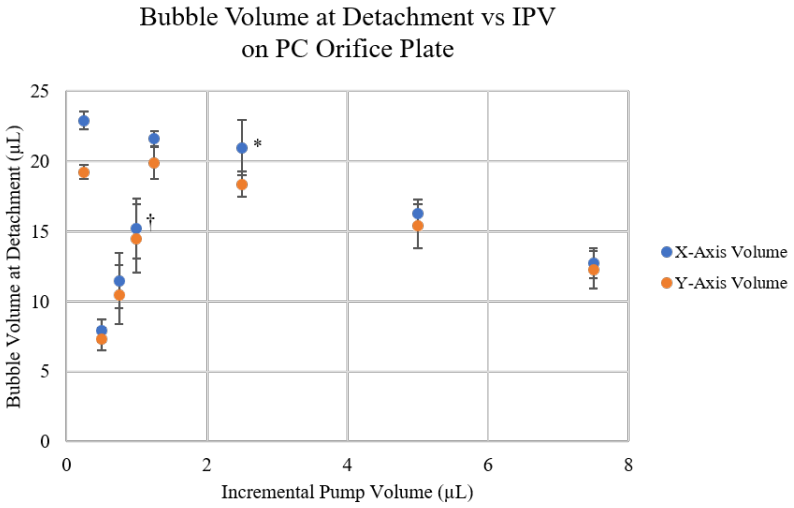

Figure 4.18: P2-1.1 Axisymmetric Bubble Volume at Detachment for X and Y Axes vs Incremental Pump Volume (IPV) on a PC Base Plate (Five Experimental Trials Except Where Marked by * or †, Room Air in Distilled Water)

*Four experimental trials conducted
†Six experimental trials conducted

The three-camera analysis was also performed on the flow rate and incremental pump volume parametric study (experiment P2-1.1) data. These results are plotted in Figure 4.19 and appear to follow the same general trend that was obtained using the axisymmetric analysis. Once again, the bubble volume increases over the FR range of 1.0 µL/s to 2.5 µL/s and then decreases as the FR continues to increase above µL/s. Figure 4.20 places the three-camera analysis results on the same chart as the axisymmetric analysis results. This chart shows alignment among most data points with the three-camera analysis being slightly lower. At FR = 1.0 µL/s and FR = 10.0 µL/s, the three-camera analysis produced results that are significantly lower than the axisymmetric results. On average, the three-camera analysis produced volume measurements that were 3.54±1.83 µL less than the averaged axisymmetric volume measurements.

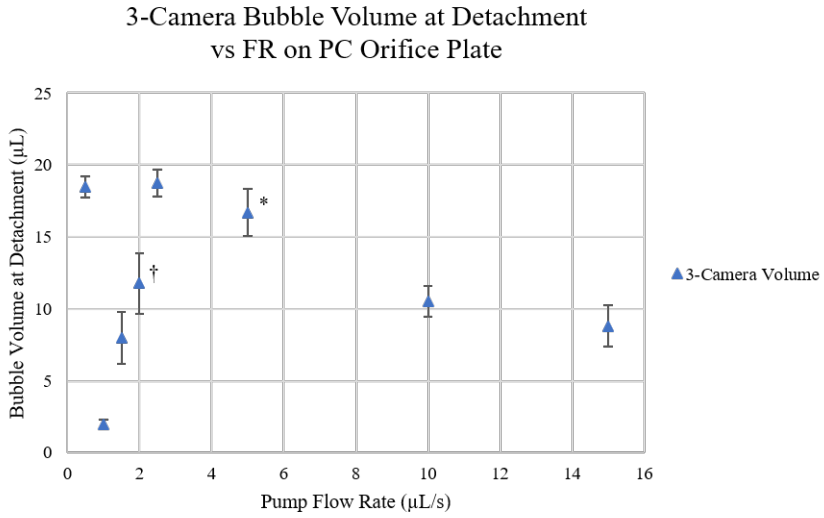

Figure 4.19: P2-1.1 Three-Camera Bubble Volume at Detachment vs Flow Rate (FR) on a PC Base Plate (Five Experimental Trials Except Where Marked by * or †, Room Air in Distilled Water)

*Four experimental trials conducted
†Six experimental trials conducted

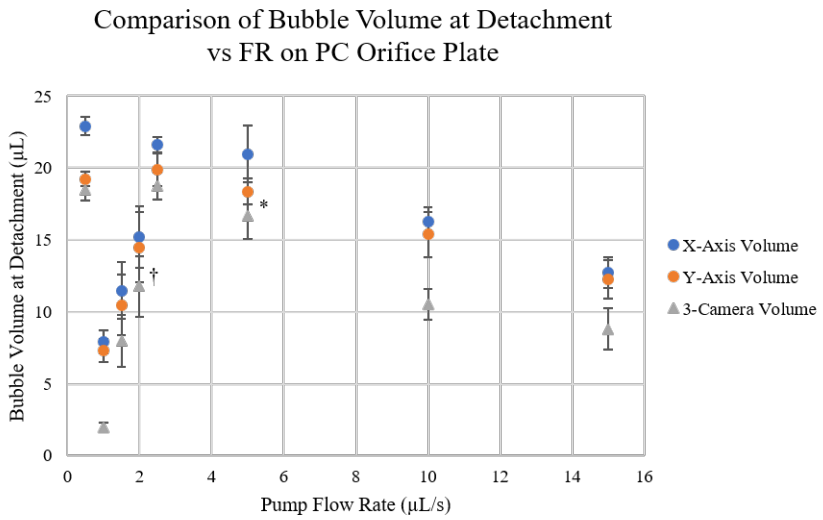

Figure 4.20: P2-1.1 Three-Camera Bubble Volume at Detachment vs Flow Rate (FR) on a PC Base Plate Compared with Axisymmetric Results (Five Experimental Trials Except Where Marked by * or †, Room Air in Distilled Water)

4.5.1.2 *P2-1.1 Flow Rate and Incremental Pump Volume Parametric Study Contact Angle Data Analysis*

The left and right contact angle at detachment were recorded for the X-axis and Y-axis cameras. Multiple trials were run at each set of test parameters, and the contact angles were averaged across these trials. Figure 4.21 shows the averaged left and right contact angles for both imaging axes. The maximum recorded contact angle was 62° and the minimum was 46°. The dotted line in the chart shows the result of a linear regression analysis performed on all contact angles (left and right). This linear trendline has a slope of 0.023±0.100 and an intercept of 53.8±0.3°. The P-value for this regression analysis was 0.816.

*Four experimental trials conducted
†Six experimental trials conducted

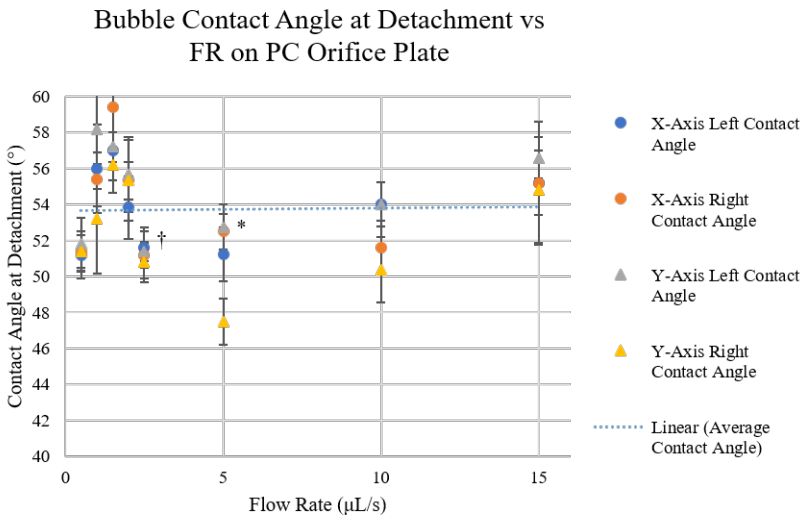

Figure 4.21: P2-1.1 Bubble Contact Angle at Detachment vs Flow Rate (FR) on a PC Base Plate with Linear Regression (Five Experimental Trials Except Where Marked by * or †, Room Air in Distilled Water)

4.5.2 P2-2.1 Polycarbonate Incremental Pump Volume Sensitivity Test Results

The polycarbonate incremental pump volume sensitivity test (experiment P2-2.1) was conducted over four days and two separate camera calibrations. The fluid used was distilled water with a temperature ranging from 23.1 °C to 25.0 °C. The gas used was air with a temperature ranging from 21.6 °C to 23.1 °C. A PC base plate was used for this experiment. The parameter that was varied was the IPV (FR and WT were held constant). The range of tested IPVs is shown in Table 3.8.

4.5.2.1 P2-2.1 Polycarbonate Incremental Pump Volume Sensitivity Test Volume Data Analysis

The bubble volume in the polycarbonate incremental pump volume sensitivity test (experiment P2-2.1) was obtained using two computer vision analyses: axisymmetric analysis (Section 3.4.2) and three-camera analysis (Section 3.4.3). The results from the axisymmetric analysis are shown in Figure 4.22 and Figure 4.23, below. These graphs show

*Four experimental trials conducted
†Six experimental trials conducted

the bubble volume, calculated through axisymmetric analysis, versus IPV. The graphs show that there was a downward trend as IPV increased from 0.2 µL to 1.0 µL. Figure 4.22 includes two sets of outlier points that do not fit this downward trend (circled in red). These outliers (at IPVs of 0.3 µL and 0.4 µL) were so far off of the general trendline that the trials were reconducted. The rerun trials showed much better agreement and are plotted in Figure 4.23, again circled in red. The bubble volume began to become level (not change) after IPV increased above 1.0 µL. The maximum average bubble volume was 23.77±0.23 µL at IPV = 0.25 µL. The minimum average bubble volume, excluding the outliers, was 12.28±0.90 µL at IPV = 5 µL. The Y-axis volume measurements were, on average, 1.23±0.97 µL less than the X-axis volume measurements.

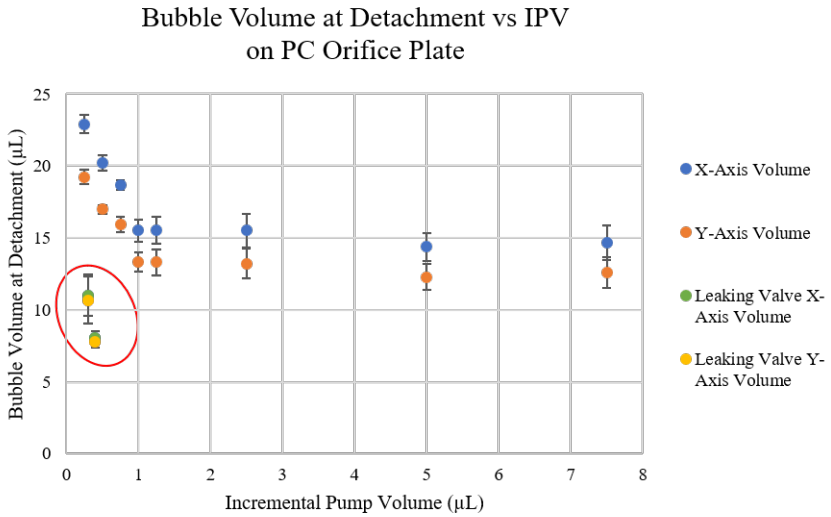

Figure 4.22: P2-2.1 Axisymmetric Bubble Volume at Detachment for X and Y Axes vs Incremental Pump Volume (IPV) on a PC Base Plate with Outlier Data Circled in Red (Five Experimental Trials, Room Air in Distilled Water)

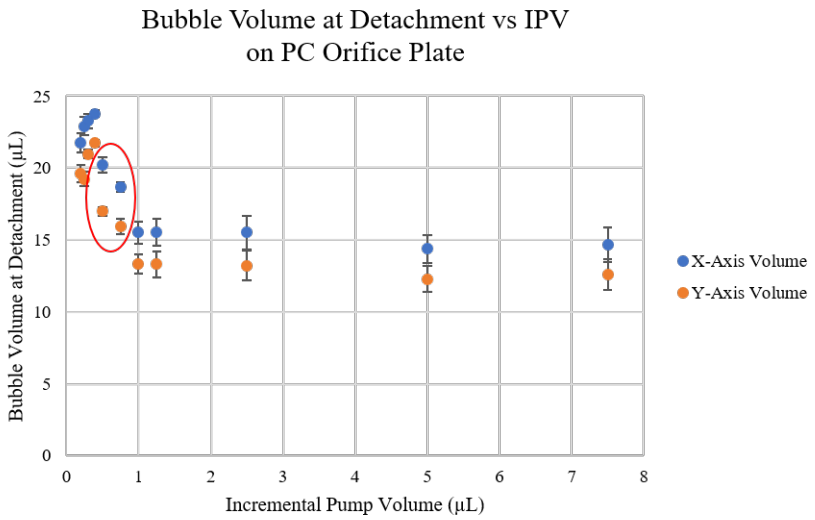

Figure 4.23: P2-2.1 Axisymmetric Bubble Volume at Detachment for X and Y Axes vs Incremental Pump Volume (IPV) on a PC Base Plate with Replaced Outlier Data Circled in Red (Five Experimental Trials, Room Air in Distilled Water)

Three-camera analysis was also performed on the polycarbonate incremental pump volume sensitivity test (experiment P2-2.1) data. These results are shown in Figure 4.24 and Figure 4.25. Once again, the outliers and replacement data are circled in these two charts. Figure 4.26 shows that the data points seem to be well aligned with the axisymmetric analysis results. The three-camera analysis produced volume data that was 1.74±1.11 µL less than the axisymmetric volume data on average.

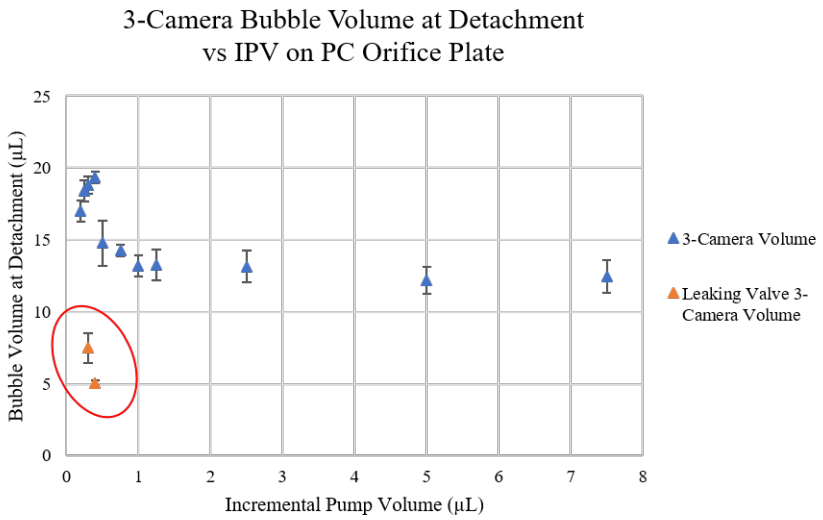

Figure 4.24: P2-2.1 Three-Camera Bubble Volume at Detachment vs Incremental Pump Volume (IPV) on a PC Base Plate with Outlier Data Circled in Red (Five Experimental Trials, Room Air in Distilled Water)

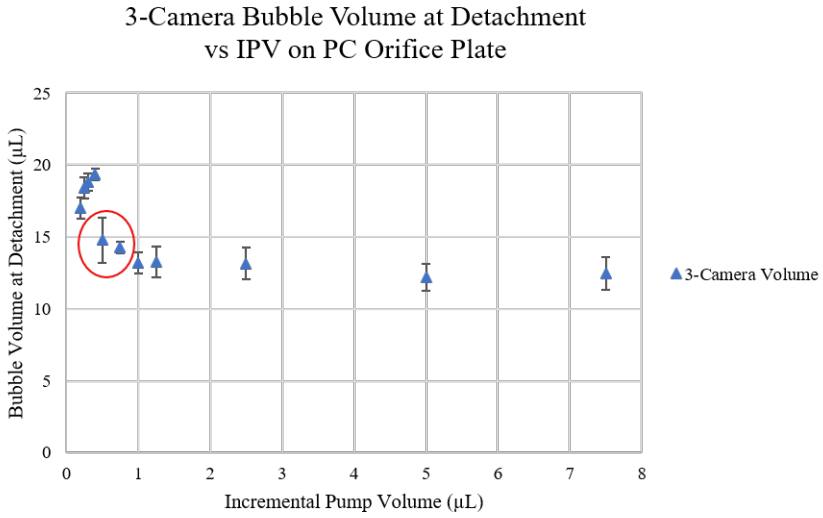

Figure 4.25: P2-2.1 Three-Camera Bubble Volume at Detachment vs Incremental Pump Volume (IPV) on a PC Base Plate with Replaced Outlier Data Circled in Red (Five Experimental Trials, Room Air in Distilled Water)

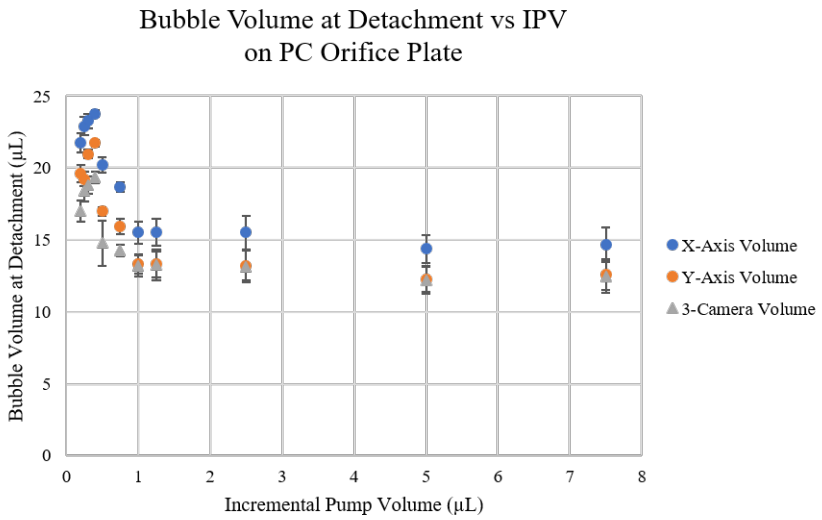

Figure 4.26: P2-2.1 Three-Camera Bubble Volume at Detachment vs Incremental Pump Volume (IPV) on a PC Base Plate Compared with Axisymmetric Results (Five Experimental Trials, Room Air in Distilled Water)

4.5.2.2 P2-2.1 Polycarbonate Incremental Pump Volume Sensitivity Test Contact Angle Data Analysis

The left and right contact angles were recorded from the X-axis images and the Y-axis images. These angles were averaged across multiple trials and plotted in Figure 4.27. The measured contact angles ranged from 44° to 56°. A linear regression analysis was applied across all measured contact angles and is also shown on the figure below. The linear trendline has a slope of -0.50±0.08 and an intercept of 50.5±0.24°. The P-value for this analysis was 5.5×10^{-9}.

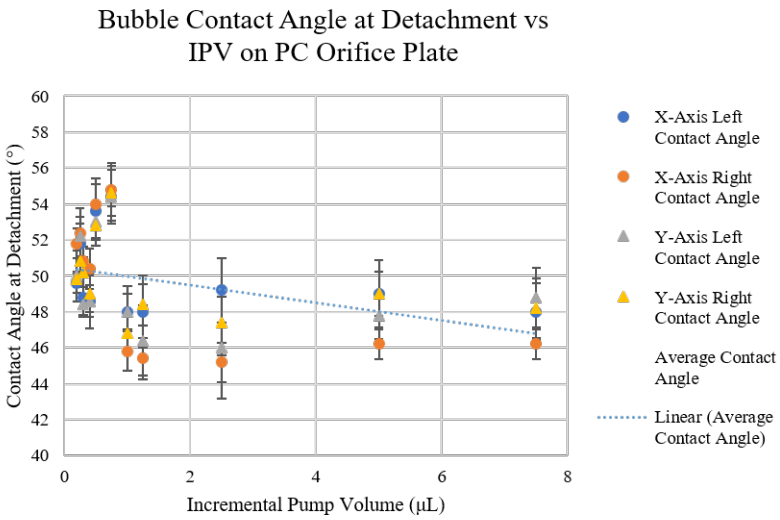

Figure 4.27: P2-2.1 Bubble Contact Angle at Detachment vs Incremental Pump Volume (IPV) on a PC Base Plate with Linear Regression (Five Experimental Trials, Room Air in Distilled Water)

4.5.3 P2-2.2 Multi-Plate Incremental Pump Volume Sensitivity Test Results

The multi-plate incremental pump volume sensitivity test (experiment P2-2.2) was conducted over six days and four separate camera calibrations. The fluid used was distilled water with a temperature ranging from 23.1 °C to 25.0 °C. The gas used was air with a temperature ranging from 21.6 °C to 23.1 °C. Three base plates were used in this experiment: PC, Al, and PTFE. SiO_2 had been planned to be used too, but manufacturing delays have prevented data collection. The parameter that was varied was the IPV. The range of the tested IPVs is shown in Table 3.9.

4.5.3.1 P2-2.2 Multi-Plate Incremental Pump Volume Sensitivity Test Volume Data Analysis

The bubble volume in the multi-plate incremental pump volume sensitivity test (experiment P2-2.2) was obtained using the axisymmetric and three-camera analyses. Figure 4.28 shows bubbles detaching from the three base plates that were tested: PC, Al, and PTFE. These time-lapse images start 25 ms before time of detachment (T_d) and end 20 ms

after detachment. These images show the visible differences in bubble shape and growth during detachment. Table 4.6 lists the measured volumes at detachment and calculated buoyant force acting on the bubbles shown in Figure 4.28. These reported volumes at detachment were obtained using the axisymmetric analysis.

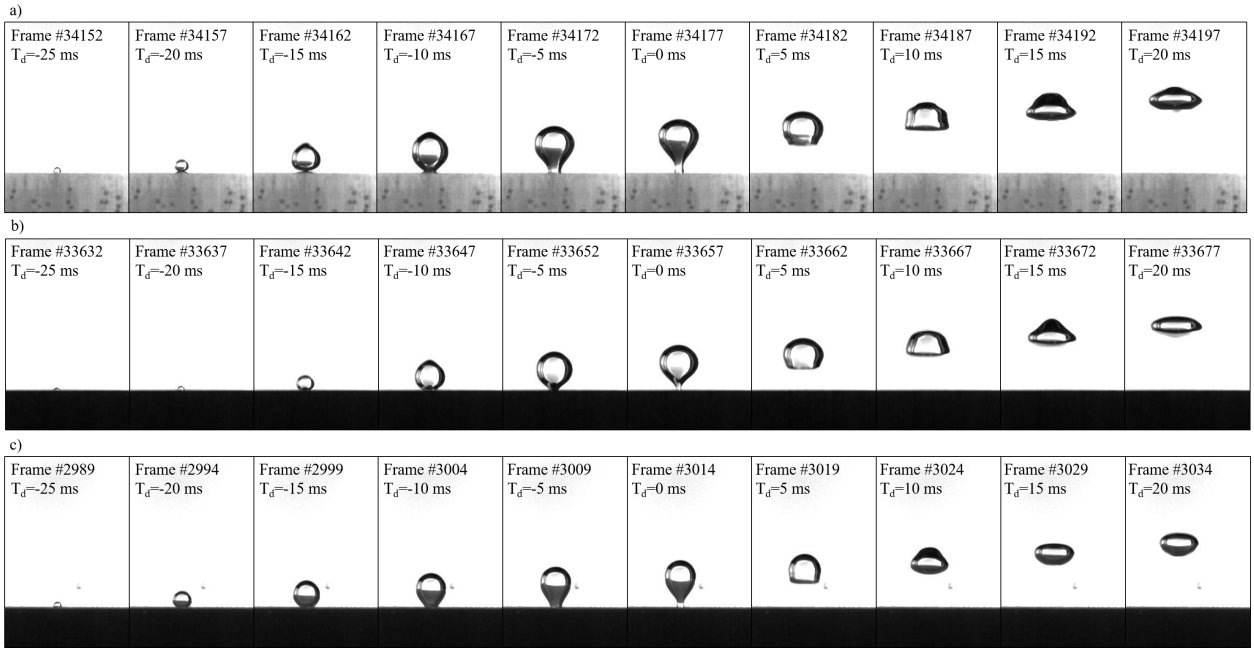

Figure 4.28: P2-2.2 Time-Lapse of Bubble Detachment for 0.2 µL Incremental Pump Volume from 25 ms Before Time of Detachment (T_d) to 20 ms After on PC (a), Al (b), and PTFE (c) Base Plates

Table 4.6: Bubble Volume, Buoyancy, and Contact Angle at Detachment on PC, Al, and PTFE Base Plates

Base Plate Material	**IPV (µL)**	**Volume at Detachment (µL)**	**F_b at Detachment (mN)**	**Contact Angle at Detachment (°)**
PC	0.2	21.76±0.65	0.213±0.006	50.3±1.2
Al	0.2	16.96±0.35	0.166±0.003	43.8±1.9
PTFE	0.2	15.52±0.19	0.152±0.002	52.5±2.1

The results from the axisymmetric analysis are shown in Figure 4.29, Figure 4.30, and Figure 4.31, these figures show the bubble volume calculated using the axisymmetric analysis versus IPV for the PC, Al, and PTFE base plates, respectively. These three sets of results show different bubble behavior across the same range of IPVs (0.2 µL to 1.0 µL).

The detachment volume of bubbles on the PC base plate are shown in Figure 4.29. The bubble volume slightly increased as IPV increased from 0.2 µL to 0.4 µL. The bubble volume then began decreasing over the IPV range of 0.4 µL to 1.0 µL. The maximum bubble volume on the PC base plate was 23.77±0.24 µL, and the minimum bubble volume was 13.33±0.66 µL. On average, the Y-axis volume measurement was 1.31±0.70 µL less than the X-axis volume measurement.

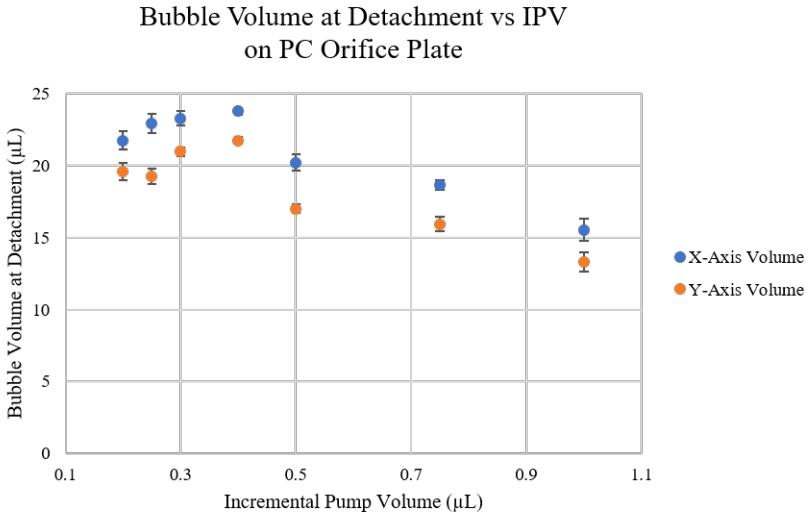

Figure 4.29: P2-2.2 Axisymmetric Bubble Volume at Detachment for X and Y Axes vs Incremental Pump Volume (IPV) on a PC Base Plate (Five Experimental Trials, Room Air in Distilled Water)

The detachment volume of bubbles on the Al base plate are shown in Figure 4.30. The bubble volume slightly increased as IPV increased from 0.2 µL to 0.5 µL. The bubble volume did not significantly change over the IPV range of 0.5 µL to 1 µL. The maximum

bubble volume on the Al base plate was 19.38±0.55 µL, and the minimum bubble volume was 15.17±0.34 µL. On average, the Y-axis volume measurement was 1.93±0.34 µL less than the X-axis volume measurement.

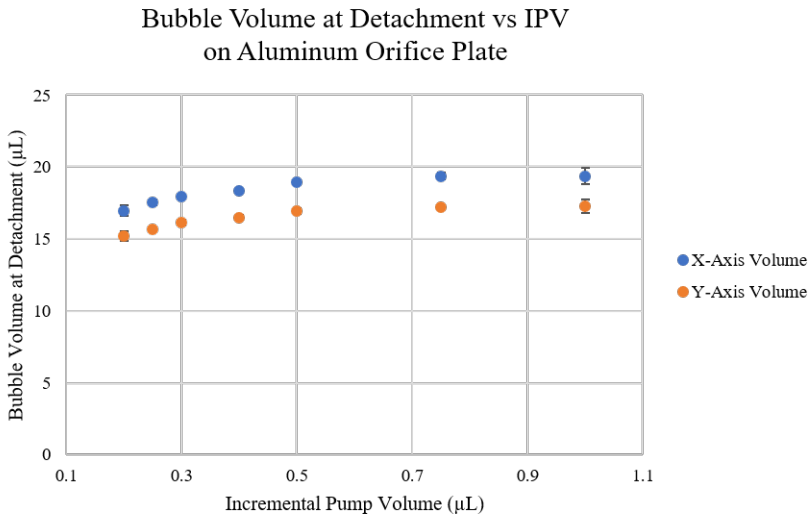

Figure 4.30: P2-2.2 Axisymmetric Bubble Volume at Detachment for X and Y Axes vs Incremental Pump Volume (IPV) on an Al Base Plate (Five Experimental Trials, Room Air in Distilled Water)

The detachment volume of bubbles on the PTFE base plate are shown in Figure 4.31. The bubble volume slightly increased across the entire range of IPV (0.2 µL to 1.0 µL). The maximum bubble volume on the PTFE base plate was 20.01±0.40 µL, and the minimum bubble volume was 14.71±0.17 µL. On average, the Y-axis volume measurement was 0.77±0.39 µL less than the X-axis volume measurement.

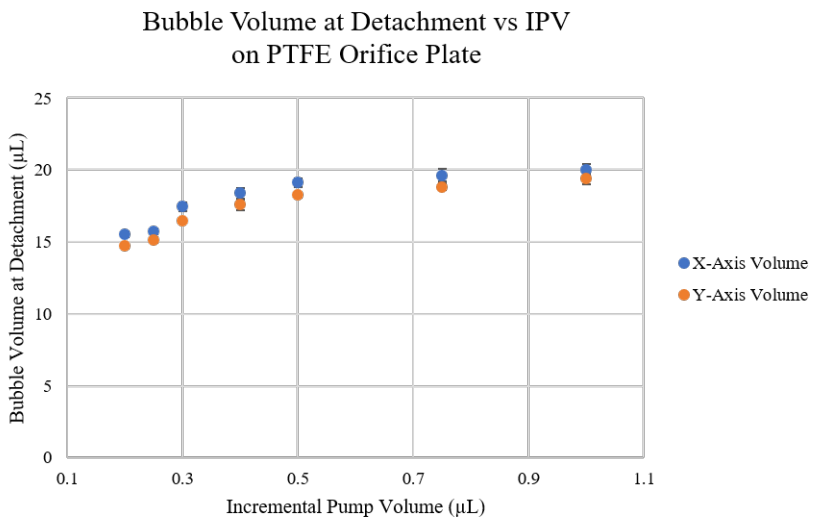

Figure 4.31: P2-2.2 Axisymmetric Bubble Volume at Detachment for X and Y Axes vs Incremental Pump Volume (IPV) on a PTFE Base Plate (Five Experimental Trials, Room Air in Distilled Water)

The three-camera analysis of the multi-plate incremental pump volume sensitivity test (experiment P2-2.2) provided the results shown in Figure 4.32, Figure 4.33, and Figure 4.34, below. Once again, there is very little disagreement between the axisymmetric analysis and the three-camera analysis. Over all trials on the PC base plate, the three-camera bubble volume was 2.37$\pm$0.90 µL less than the averaged axisymmetric bubble volume. Over all trials on the Al base plate, the three-camera bubble volume was 0.49$\pm$0.33 µL less than the averaged axisymmetric bubble volume. Over all trials on the PTFE base plate, the three-camera bubble volume was 2.17$\pm$0.37 µL less than the averaged axisymmetric bubble volume.

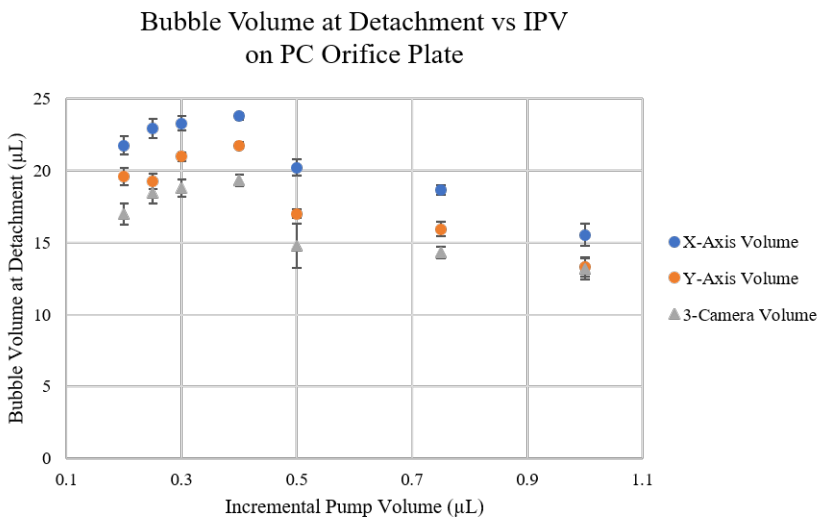

Figure 4.32: P2-2.2 Three-Camera Bubble Volume at Detachment vs Incremental Pump Volume (IPV) on a PC Base Plate Compared with Axisymmetric Results (Five Experimental Trials, Room Air in Distilled Water)

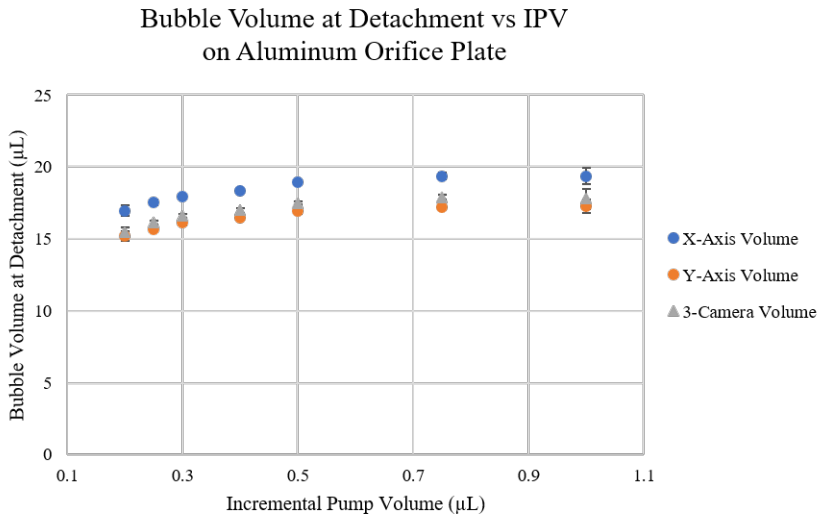

Figure 4.33: P2-2.2 Three-Camera Bubble Volume at Detachment vs Incremental Pump Volume (IPV) on an Al Base Plate Compared with Axisymmetric Results (Five Experimental Trials, Room Air in Distilled Water)

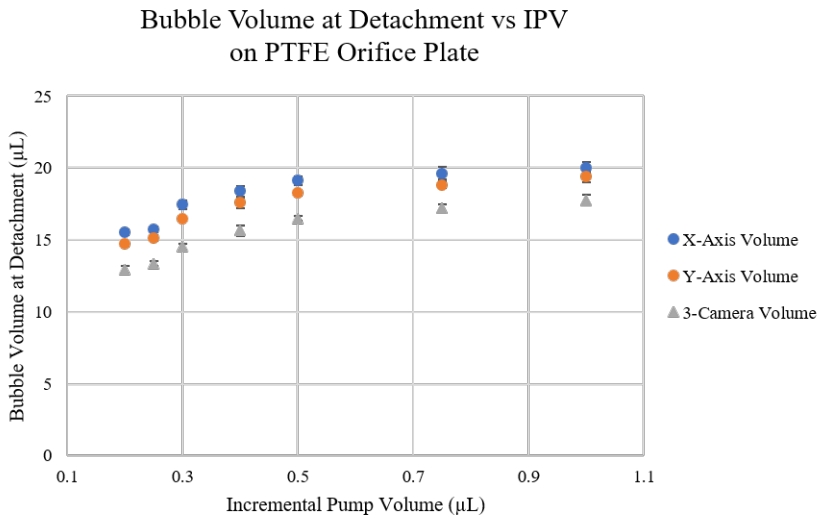

Figure 4.34: P2-2.2 Three-Camera Bubble Volume at Detachment vs Incremental Pump Volume (IPV) on a PTFE Base Plate Compared with Axisymmetric Results (Five Experimental Trials, Room Air in Distilled Water)

4.5.3.2 P2-2.2 Multi-Plate Incremental Pump Volume Sensitivity Test Contact Angle Data Analysis

The analysis of the multi-plate incremental pump volume sensitivity test (experiment P2-2.2) was continued by examining the left and right contact angles in the X-axis and Y-axis images. These data points are plotted for PC, Al, and PTFE in Figure 4.35, Figure 4.36, and Figure 4.37, respectively. The measured contact angles on the PC base plate ranged from 46° to 57°. A linear regression analysis was applied to these contact angles and was also plotted on Figure 4.35. The slope of this trendline was found to be -1.11±0.84 with an intercept of 51.4±0.5°. The P-value for this analysis was 0.19.

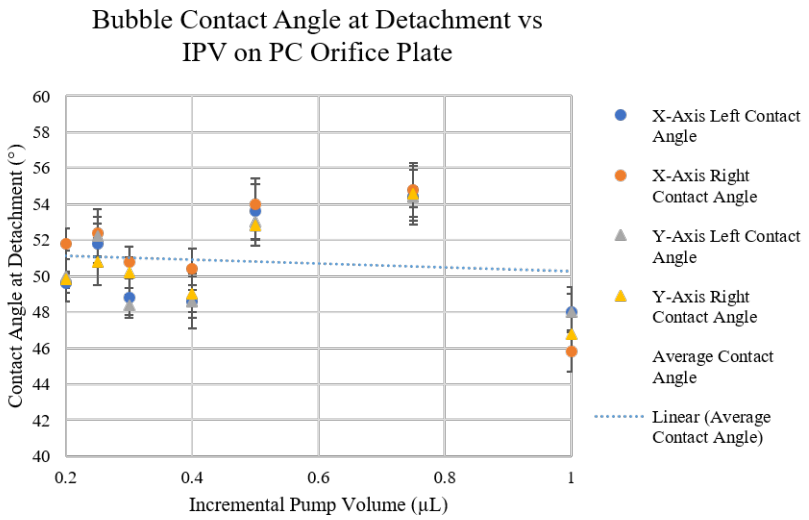

Figure 4.35: P2-2.2 Bubble Contact Angle at Detachment vs Incremental Pump Volume (IPV) on a PC Base Plate with Linear Regression (Five Experimental Trials, Room Air in Distilled Water)

The measured contact angles on the Al base plate ranged from 40° to 48°. A linear regression analysis was applied to these contact angles and was also plotted on Figure 4.36. The slope of this trendline was found to be -0.69±0.55 with an intercept of 43.2±0.3°. The P-value for this analysis was 0.22.

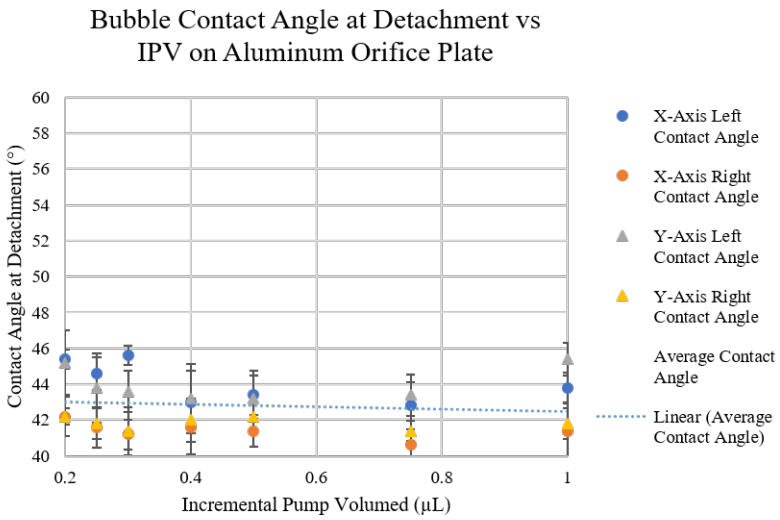

Figure 4.36: P2-2.2 Bubble Contact Angle at Detachment vs Incremental Pump Volume (IPV) on an Al Base Plate with Linear Regression (Five Experimental Trials, Room Air in Distilled Water)

The measured contact angles on the PC base plate ranged from 45° to 55°. A linear regression analysis was applied to these contact angles and was also plotted on Figure 4.37. The slope of this trendline was found to be -3.20±0.52 with an intercept of 52.5±0.33°. The P-value for this analysis was 5.4×10^{-9}.

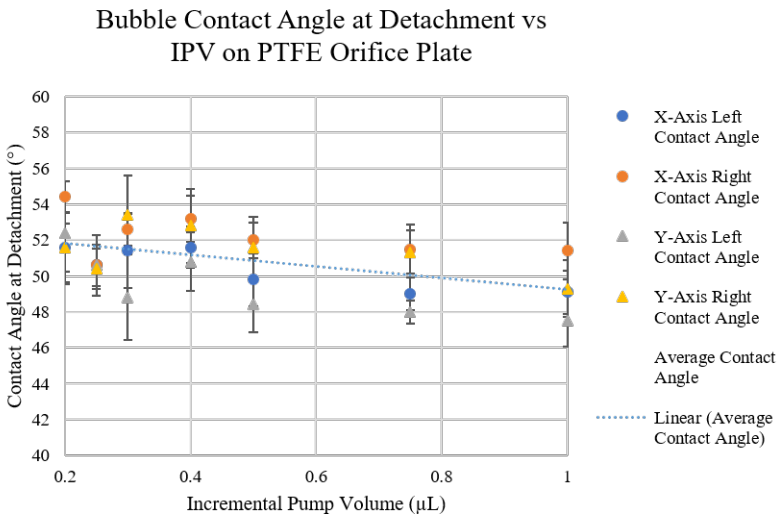

Figure 4.37: P2-2.2 Bubble Contact Angle at Detachment vs Incremental Pump Volume (IPV) on a PTFE Base Plate with Linear Regression (Five Experimental Trials, Room Air in Distilled Water)

In Figure 4.38, the average bubble contact angles for each base plate (PC, Al, and PTFE) are plotted with their respective linear regression trendlines. The trendlines for PC and Al appear significantly flatter than the trendline for PTFE. The average contact angle for Al (42.8°) is also significantly lower than that of PC (50.8°) or PTFE (50.7°).

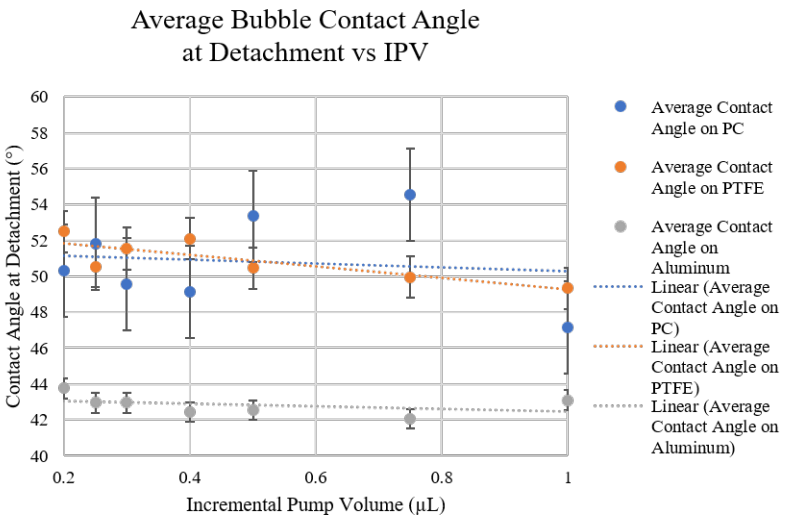

Figure 4.38: P2-2.2 Average Bubble Contact Angles at Detachment (Left and Right) vs Incremental Pump Volume (IPV) on a PC Base Plate with Linear Regressions (Five Experimental Trials, Room Air in Distilled Water)

S

5. DISCUSSION

The quiescent bubble detachment experiment platform has been designed to operate as a laboratory-based benchmark test for partial gravity CFD model validation. Much research has been conducted on fluids in Earth's gravity and in microgravity, but little to none has been conducted in partial gravity. As a result, no validated CFD models exist for two-phase fluids in this regime. This experiment will be used as a 1 g measurement system for validation of these future models and will also be used to develop a flight experiment for benchmarking at reduced gravity levels. The laboratory-based experimental platform has been fully designed and rigorously tested. Analysis of the platform has led to a number of revelations which are discussed in this section. The experimental platform was iteratively designed in two phases: Phase 1 and Phase 2. The Phase 1 design was used as a proof of concept and to generate informed design decisions for the Phase 2 design. The Phase 2 experimental platform was the final configuration and was used to gather the benchmark experimental data needed to validate bubble detachment CFD models in 1 g. Two additional categories of tests were conducted: Sessile drop tests and camera calibration tests. The Sessile drop test was used to characterize the orifice plate surface energies. The camera calibration tests were used to obtain accurate measurements of objects using computer vision algorithms.

5.1 Sessile Drop Test Discussion

The Sessile drop test results are shown in Table 4.2 in Section 4.2 and were compared to published surface energies for the same materials. The surface roughness of a material can have a large effect on the surface energy of the material and is the reason for the large range of values for the SiO_2, PC, and PTFE. The surface energy of Al was reported as a single number in the literature, but it was assumed that it too had a significant range of surface energies. With this considered, all measured contact angles and calculated

surface energies were in good agreement with the published values. These calculated surface energies are to be used in CFD model validation.

5.2 Camera Calibration Discussion

Camera calibration tests were developed to remove distortion from images and to calculate image SFs. The image SF is the ratio of inches per pixel in the image (in/px). This calculation was made by using computer vision algorithms to measure the diameter of high precision ball bearings. The SF is highly dependent upon the distance of the object to the camera. The mean SF for each camera in each calibration test was compiled along with their standard deviation. Dividing the standard deviation of the SFs, an estimate of the measurement error, by the average SF provided a percent error of 3.52% which is actually the accuracy of the imaging system. This error is significantly low and would account for only ± 0.70 µL for a bubble that was 20 µL in total volume. This increased uncertainty in volume measurements is a result of error propagation and is unavoidable. The addition of the second camera on an orthogonal axis doubles the number of measurements made and therefore reduces the sampling error. The camera calibration test was accepted if the reprojection error was found to below a threshold of 0.220. This heuristic is somewhat arbitrary, but was the value that was found to be rigorous yet achievable. It was often the case that the reprojection error was much lower, such as 0.150 for the Z-axis camera in Table 4.3.

5.3 Phase 1 Discussion

The Phase 1 experiments (P1-1.1 and P1-1.2) were conducted to determine the usefulness and reliability of the selected system architecture for the proposed quiescent bubble detachment experiment. The results from these two experiments showed that the design was sound and that useful data could be collected. The preliminary sensitivity test (experiment P1-1.1) revealed a number of critical experimental parameters. It showed that the optimal FR was 1.0 µL/s, that the optimal IPV was 0.25 µL, that the minimum WT

needed for quiescent bubble detachment was 2 seconds. The repeatability analysis experiment (P1-1.2) was used to determine the repeatability of the bubble detachment under optimal parameters determined by the previous experiment. It was found that the average bubble volume was 30.4 µL $\pm$ 3.9 µL. The PE for the bubble detachment volume in this experiment was 12.8%, which is quite high. The bubble contact angle at detachment was also measured and found to be 55.1° $\pm$ 5.3°, with a PE = 9.6%.

There were, however, problems with the Phase 1 design that were encountered. Bubble volume could not be measured by computer algorithm methods due to poor clarity in the fluid chamber walls. The extruded PC plastic was very hazy and had large, visible distortions. Instead the infusion pump was used to measure bubble volume. This method was somewhat consistent, but was vulnerable to measurement error due to possible leaks in the gas injection system. Even small nL/s leaks could cause significant volume measurement error due to the long time period of bubble formation. It was suspected that switching to a vision-based measurement system could reduce the PE for the bubble volume measurements. This problem was addressed in the redesign of the fluid chamber for Phase 2.

The validation of CFD models, while outside of the scope of this design project, have already entered the preliminary stages. Initial CFD model validation has begun using the data captured in experiment P1-1.2. The data results have been compared to the CFD results, both of which are tabulated in Table 4.5.

5.4 Phase 2 Discussion

In Phase 2, experiments were conducted to determine the effects of FR and IPV on the bubble volume and contact angle at detachment. Three experiments were conducted and their results are reported in Section 4.5.

5.4.1 Experiment P2-1.1 Discussion

The first Phase 2 experiment, flow rate and incremental pump volume parametric study (experiment P2-1.1) examined the change in bubble volume and contact angle as a function of a changing FR and IPV. This test was only conducted on the PC orifice plate since it included two independent variables. Typically, only one independent variable is changed in an experiment, but in this case both FR and IPV were changed, while the ratio between FR and IPV was kept constant. The results of this test are shown on Figures 4.17−4.21. The bubble volume analysis showed good agreement between the two methods of volume calculation (axisymmetric and three-camera analysis). The bubble volume seems to have a positive correlation to FR and IPV over small FR and IPV, but then a negative correlation as FR and IPV continue to increase. The nature of this relationship cannot be decoded until experiments with a single independent variable are run over these conditions. In addition, the data point for the lowest FR and IPV is very high compared to the adjacent measurements. The cause of this is also unknown until further testing is performed. The contact angle analysis for this experiment shows a wide spread of contact angles from $46^\circ - 62^\circ$. The contact angles did not appear to have any relationship to changes in FR and IPV. This statement was bolstered by the regression analysis which found a linear fit with a slope of 0.023 and P-value of 0.816. Such a high P-value strongly indicated that the null hypothesis (that the independent and dependent variables are not related) cannot be rejected. As a result, the data does not show any relationship between bubble contact angle at detachment and FR and IPV across the tested range.

5.4.2 Experiment P2-2.1 Discussion

The second Phase 2 experiment, polycarbonate incremental pump volume sensitivity test (experiment P2-2.1) was conducted to determine the effects of IPV on bubble volume and contact angle at detachment. This experiment was conducted on the PC orifice plate with an IPV range of 0.2 µL to 7.5 µL. The results of this experiment are shown in Figures

4.22−4.27. In this experiment there was a downward trend in bubble volume at detachment over the range of 0.2 µL to 1.0 µL, with the exception of two data points (circled in red on Figures 4.22 and 4.24) that were seemingly outliers. The experiment operators suspected that a leak had developed in the gas pumping system and that those data points were not representative of the relationship between IPV and bubble volume. To test this hypothesis, the investigators disassembled and reassembled the apparatus before reconducting those trials. The rerun trial data is shown in Figures 4.23 and 4.25, also circled in red. The rerun trials show much better agreement with the rest of the data set, leading to the conclusion that the leak or other anomaly had been fixed. Comparison of the three-camera analysis and the axisymmetric analysis, once again, showed good agreement with only a 1.74 µL volume differential between the two methods. An important observation was the leveling off of the bubble volume at detachment once IPV was greater than 1.0 µL. This leveling off was a result of the bubble detachment occurring during a pump cycle instead of a wait time. Since FR was held constant in this test, any IPV $>$ 1.0 µL should have approximately the same volume at detachment. Lastly, the contact angles were analyzed for this experiment and the results were plotted in Figure 4.27. A linear regression analysis was applied to these data points and found an inverse relationship between IPV and bubble contact angle. The slope of the linear trendline was -0.495$\pm$0.081 with a P-value of 5.5×10^{-9}. This is a clear indication that there is an inverse relationship between contact angle and IPV, but the linearity of the relationship requires additional investigation. Further tests could be used to support or challenge this assumption.

5.4.3 Experiment P2-2.2 Discussion

The multi-plate incremental pump volume sensitivity test (experiment P2-2.2) was a performed based upon the results of P2-2.1, which showed that bubble volume at detachment was not changed once IPV was greater than 1.0 µL. In this experiment the IPV was tested over a range of 0.2 µL to 1.0 µL on three separate orifice plates: PC, Al, and PTFE. The data from P2-2.1 was used as the results for the PC orifice plate in this experiment

and was plotted over the smaller range of IPV in Figures 4.29, 4.32, and 4.35. The bubble volume at detachment on the PC base plate slightly increased from 20.7 µL to 22.8 µL before significantly decreasing to 14.4 µL. The three-camera analysis showed the same trend and was on average 2.37 µL less than the volume calculated using the axisymmetric analysis. At this point in the experiment, the investigators began to notice a suspicious pattern: the Y-axis volume data was always less than the X-axis volume data. In the PC test data, the Y-axis measured volumes at 1.31 µL less than the X-axis data; the same was true in the P2-1.1 experiment where the difference was 1.46 µL. The experiment continued with extra attention on this observation.

The next base plate that was tested was the Al base plate. The results of this test are shown in Figures 4.30, 4.33, and 4.36. The bubble volume at detachment on the Al base plate slightly increased from 16.1 µL to 17.9 µL over a range of IPVs from 0.2 µL to 0.5 µL. Above 0.5 µL, IPV seems to have minimal effect on bubble volume. At IPV = 1.0 µL, bubble volume was 18.3 µL. The Y-axis camera was still measuring volumes below the measurements on the X-axis camera; this time 1.93 µL below. The three-camera analysis also produced a smaller volume on average: 0.49 µL smaller.

The PTFE was the last base plate that was tested and the results are shown on Figures 4.31, 4.34, and 4.37. Investigators had suspicions about how the measurements from the Y-axis camera were consistently lower than those made from the X-axis camera and they decided to switch the camera positions during this test to eliminate the possibility that one of the cameras had a defect. The bubble volume results showed, once again, a clear difference between X-axis measurements and Y-axis measurements, with Y-axis measurements still 0.77 µL smaller. These results and test have indicated to the investigators that the problem is not internal to the camera-lens system, but is instead a result of the fluid chamber or calibration method. The three-camera volume analysis was also found to be 2.17 µL lower than the axisymmetric results. Ultimately, it is suspected that the fluid chamber walls (which are not present during camera calibration) are slightly

thicker along one of the axes and are therefore causing additional extrinsic distortions that the camera calibration has not corrected for. The mitigating factor, which has not yet been tested, is to conduct the camera calibration with the checkerboard and ball bearings inside the filled fluid chamber. This would ensure the that all extrinsic distortions are calculated and properly remove. Since this experimental platform will continue to be used for CFD model validation, performance of proper calibration procedures should be further investigated.

Next the bubble contact angle at detachment was analyzed for the PC, Al, and PTFE base plates. These results are shown in Figures 4.35−4.38. The relationship between bubble contact angle and IPV on the PC base plate was found to be quite weak. A linear regression analysis of the data points found an inverse relationship with a slope of -1.11$\pm$0.84, with a P-value of 0.19. These results show that a weak relationship may exist, but that further testing is needed before the null hypothesis can be rejected with confidence. A similar result was found on the Al base plate. The contact angle regression analysis for bubbles on Al found a slope of -0.69$\pm$0.55, with a P-value of 0.22. This high P-value indicates that the null hypothesis (no relationship between IPV and contact angle) cannot be rejected with confidence. The data for the contact angles on the PTFE base plate, however, were more conclusive. The same regression analysis showed a clear inverse relationship between IPV and contact angle on PTFE. The slope of the linear fit was -3.20$\pm$0.52, with a P-value of 5.4×10^{-9}. This analysis shows that the trendline is a good fit over the range of tested IPVs. The results of each of these analyses are plotted together in Figure 4.38. This chart shows that the surface material and surface energies do play a role in the bubble contact angle during detachment, while IPV has almost no effect. An interesting result was that the PC and PTFE results were at about the same contact angle (approximately 51°), but the two materials have greatly differing surface energies. In fact, the surface energy of Al was found to be between that of PC and PTFE, but its contact angles were significantly lower at approximately 43°.

5.5 Future Work

This experimental platform will be used to continue a number of projects in the AHSL fluid physics research group. Among them are CFD model validation and potential bubble detachment flight experiments either on the ISS or on the lunar surface. These continuing research projects have directly benefited from the data and research behind this project.

5.5.1 CFD Model Development and Validation

CFD models for bubble detachment are currently being developed by doctoral student Paul Burke in the AHSL fluids research team. Initial models have been designed and compared with the Phase 1 experimental data. This initial comparison was the first step toward validation and relied upon comparison of bubble volume and contact angle at detachment. This comparison showed reasonable agreement with detachment volume and contact angle. The model is currently being improved in preparation for comparison with the Phase 2 experimental results.

5.5.2 Flight Experiments

The AHSL plans to design, build, and fly a quiescent bubble detachment experiment in a reduced gravity environment. Two options for flight experiments have been investigated: one in artificial partial gravity in a centrifuge on the ISS and the other in steady-state partial gravity on the lunar surface. Flight experiments are the only way to conduct experiments in long duration reduced gravity. Conducting a bubble detachment experiment in these gravity regimes will allow researchers to validate CFD models in reduced gravity, driving development of innovative fluid systems for space applications. The laboratory-based experimental platform is too large to fly as a flight experiment in its current configuration, but the development of the systems needed to create such an experiment has raise the TRL of the flight experiment from TRL 2 (concept) to TRL 4 (laboratory validation).

As progress is made toward a future flight experiments, further testing of the breadboard experiment will be required. For instance, if a centrifuge experiment is the selected approach, the laboratory experiment will need to be adapted and tested in a centrifuge in 1 g before the design of the flight experiment. A lunar experiment would require testing in cold, hot, and dusty environments. These and many other challenges will need to be addressed when validating the experimental design for a flight experiment. The research in this thesis is not complete enough to define all requirements for a flight experiment, but some key requirements were developed. Table 5.1 provides a list of the recommended requirements that were developed as a part of this thesis that should be included as requirements for any potential flight experiment. It is possible that other design solutions exist for creating this flight experiment through a novel approach, however, any flight experiment that does not meet these recommended requirements must be retested and validated through TRL 4 to ensure that it is capable of collecting the requisite data.

Table 5.1: Recommended Design Requirements for Future Two-Phase Bubble Detachment Flight Experiments

Requirement Name	**Definition**
Fluid Chamber Clarity	Clear plastic with low distortion, polycarbonate or acrylic
Fluid Chamber Dimensions	A minimum of 2″ x 2″ x 2″
Gas Pumping Rate	Gas must be capable of being pumped at 0.1 µL/s or lower
Working Fluids	Distilled water and air work well and are low hazard
Base Plate Exchangeability	Orifice plates should be interchangeable or use multiple test chambers
Base Plate Materials	Base plates should have a variety of surface energies ranging from 20 mJ/m^2 to 55 mJ/m^2
Camera Frame Rate	Cameras should capture at a minimum of 250 FPS
Number of Cameras	A minimum of 2 cameras
Camera Orientation	Cameras should be aligned orthogonal to each other and level with the base plate
Imaging Resolution	224 x 342 px is sufficient if cameras are placed 2″ from the orifice, this correlates to a 0.002″/px scale factor

One potential future partner of the flight experiment phase of this research is Techshot,

Inc. Techshot operates a small centrifuge on board the ISS call the MVP (see Figure 2.2), which could provide the artificial gravitational environment needed for reduced gravity experimental data collection. Initial designs have been developed to scale the breadboard experimental platform for integration into the Techshot MVP centrifuge module. Figure 5.1 and Figure 5.2, below, show a preliminary design for the flight experiment.

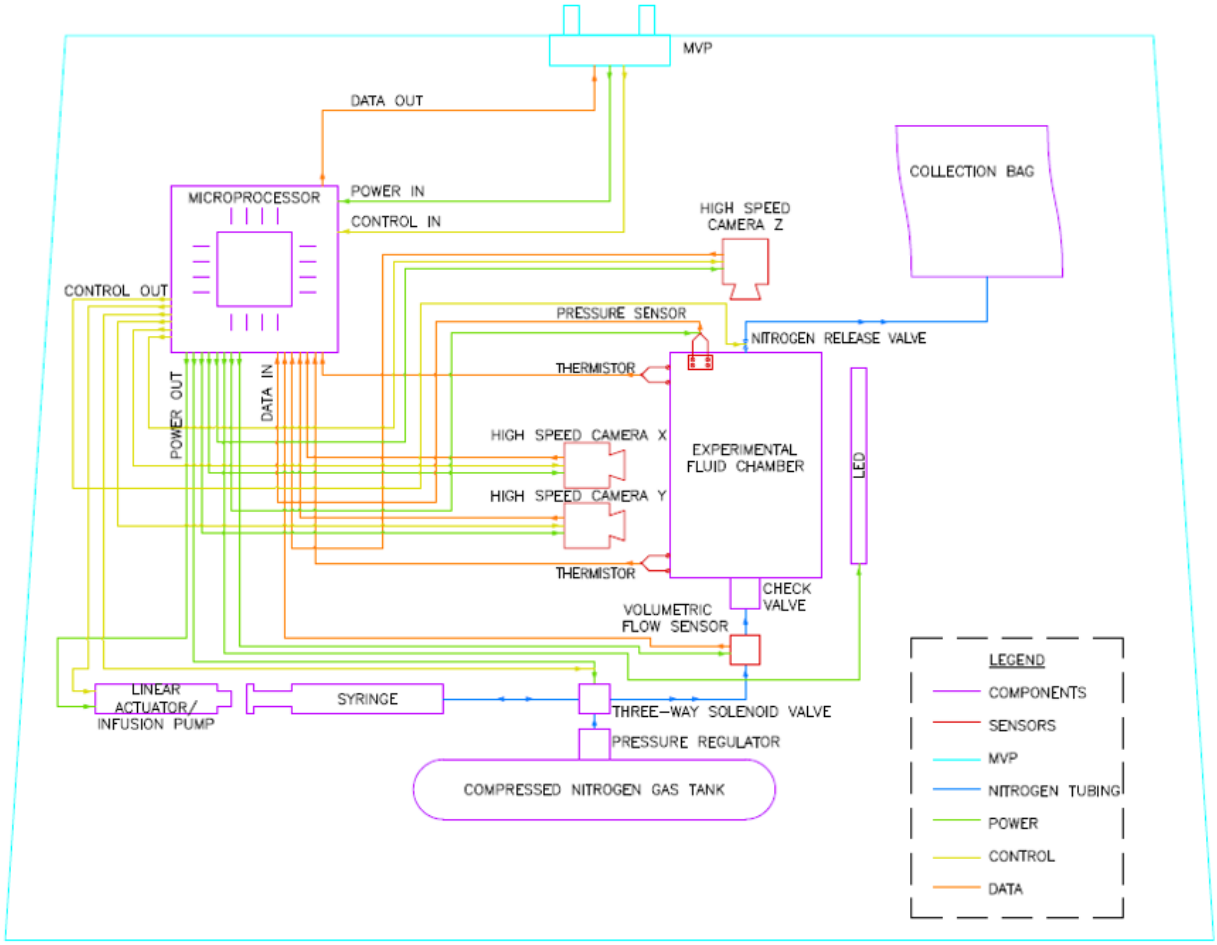

Figure 5.1: Preliminary Systems Diagram for a Bubble Detachment Experiment in the Techshot MVP Module on the ISS

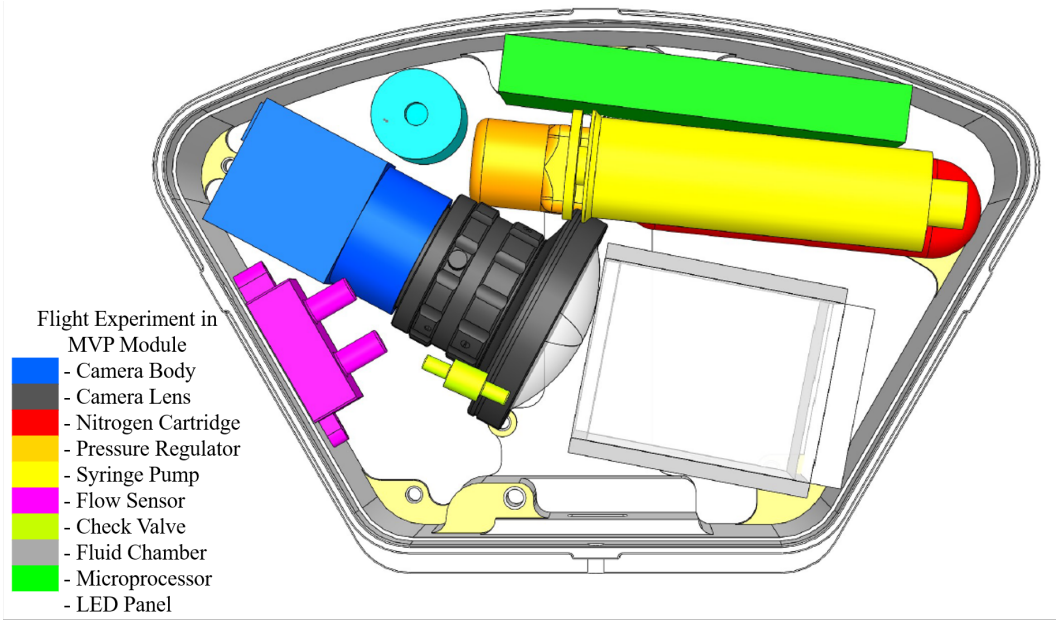

Figure 5.2: Preliminary CAD Drawing for a Bubble Detachment Experiment in the Techshot MVP Module on the ISS

6. CONCLUSIONS

In this thesis project a two-phase bubble formation and detachment breadboard experiment was designed and tested for the purposes of validating a 1 g CFD model. This data collected in this project will be used as a benchmark for model validation in 1 g, and the information gathered has been translated toward requirements for future flight experiments. The experimental platform has raised the TRL of the research project from TRL 2 to TRL 3, paving the way for a future flight experiment.

The design process has revealed a number of critical design parameters for creating a reliable bubble detachment experiment. The fluid chamber clarity and imaging system calibration are critical for accurate volume measurements. The designed imaging system has excellent spatial and temporal resolution for the quiescent processes being observed. However, the calibration protocol could be improved to improve accuracy. Calibration objects should be placed inside of the filled fluid chamber to accurately measure the extrinsic distortion of the images. The current method has produced consistent deviations between X-Axis and Y-Axis measurements of bubble volume. Current methods have produced an accuracy that is 3.52% (measured as a percent error). This error should be further reduced by improving the calibration protocol, and therefore increasing the accuracy of the imaging system.

The three-camera volume analysis has produced results comparable to those produced using an axisymmetric assumption. The incorporation of the Z-Axis camera was found to be a very difficult task that was never successfully achieved. When the Z-Axis camera received enough light to be properly imaged, the X-Axis and Y-Axis images were washed out. This was the case for all apertures available on the camera lenses. Changing camera shutter speed (increasing shutter speed for X-Axis and Y-Axis cameras) could be a solution to this problem, but the current cameras were not able to do this. Instead, the Z-Axis image was approximated as an ellipse to test the reliability of this algorithm

compared to the axisymmetric analysis. The results had good agreement with the axisymmetric results, and as such, these results did not add any significant new information. Therefore, it is not the recommendation of this research to use a three-camera system when the same results can be achieved with only two cameras.

The fluid chamber and pumping system were refined over the course of testing the apparatus. The Phase 1 fluid chamber showed the drastic loss in image quality that can be experienced when a poor clarity plastic is used. The solution was achieved by sourcing high clarity PC. Lessons were also learned in the design of the pumping system, which began to leak during one test. To fix the leak, the investigators removed all fittings and piping and reassembled the system. Next, the effected trials were rerun and the data appeared much cleaner. Ultimately, limiting the points of failure could greatly reduce the chances of more leaks occurring. The infusion pump and gastight syringe worked perfectly over the course of the experiments in Phase 1 and Phase 2.

The experiments conducted were analyzed to examine consistency of results, but not to draw conclusions on physical processes. The results from the two Phase 1 experiments identified the optimal configuration for the experimental tests that followed in Phase 2. In the three Phase 2 experiments it was found that bubble contact angle at detachment is mostly independent of IPV on the range that was tested (with the exception of bubbles on the PTFE base plate). The analysis process revealed very weak correlations, which conforms with theory. Bubble contact angle should be indicative of surface tension forces, not kinetic forces. Further study of bubbles on different surfaces should help illuminate the true relationships between bubble contact angle at detachment and surface tension forces. Tests over a broader range of surface energies (and therefore surface tensions) are already planned for the future in the AHSL. One such test will utilize a Quartz (SiO_2) base plate, and has a much higher surface energy. The bubble volume results showed a variety of different trends for different IPV and FR ranges. These results do not lead to any particular conclusion aside from the precision and accuracy of the device as a

whole. The volume measurements conducted using the current methods only show a 1.42% error between measurements. This error represents the precision of the system, while the percent error for the calibration represents the accuracy.

The breadboard experimental apparatus has successfully been developed and tested and the future work shall be to further improve the calibration procedures (and therefore the instrument accuracy) and to use the results to benchmark newly developing two-phase CFD models. Recommended requirements for a future flight experiment have also been provided as a conclusion to this design project. In conclusion, this project has helped to move research forward in several aspects toward the goal of partial gravity two-phase computational models.

REFERENCES

[1] L. Peterson, "Environmental control and life support system (eclss)," in *System Engineering Workshop, Life Sciences Department*, ISU SSP, Ames Research Center, International Space University, 2009.

[2] D. A. Fester, A. J. Villars, and P. E. Uney, "Surface tension propellant acquisition system technology for space shuttle reaction control tanks," in *11th American Institute of Aeronautics and Astronautics and Society of Automotive Engineers, Propulsion Conference*, no. 75-1196, (Anaheim, CA), NASA, AIAA, Oct. 1975.

[3] F. Miller, C. Niederhaus, K. Barlow, and D. Griffen, "Intravenous solutions for exploration missions," in *45th AIAA Aerospace Sciences Meeting and Exhibit*, (Reno, NV), NASA Glenn Research Center, AIAA, Jan. 2007.

[4] C. Panzarella, "Microfluidic biochip design," in *Strategic Research to Enable NASA's Exploration Missions Conference and Workshop: Poster Session*, vol. 2, pp. 307–308, NASA Glenn Research Center, NASA Glenn Research Center, Aug. 2004.

[5] M. Ababneh, C. Tarau, W. Anderson, J. Farmer, and A. Alvarez-Hernandez, "Hybrid heat pipes for lunar and martian surface and high heat flux space applications," in *46th International Conference on Environmental Systems*, (Vienna, Austria), ICES, July 2016.

[6] S. Ostrach and Y. Kamotani, "Surface tension driven convection experiment (stdce)," resreport 198476, NASA Lewis Research Center, June 1996.

[7] R. Zurawski, "The iss fluids and combustion facility-microgravity combustion science and fluid physics research capability," in *Conference and Exhibit on International Space Station Utilization*, no. 211308, NASA, AIAA, Dec. 2001.

[8] R. Kumar and N. K. Kaloor, "The formation of bubbles and drops," *Advances in Chemical Engineering*, vol. 8, pp. 255–368, 1970.

[9] A. Dhruv, E. Balaras, A. Riaz, and J. Kim, "A formulation for high-fidelity simulations of pool boiling in low gravity," *International Journal of Multiphase Flow*, vol. 120, 2019.

[10] H. K. Nahra and Y. Kamotani, "Bubble formation from wall orifice in liquid cross-flow under low gravity," *Chemical Engineering Science*, vol. 55, pp. 4653–466, Jan. 2000.

[11] S. Qiao, D. Mena, and S. Kim, "Inlet effects on vertical-downward airwater two-phase flow," *Nuclear Engineering and Design*, vol. 312, pp. 375–388, Feb. 2017.

[12] K. Mishima and M. Ishii, "Flow regime transition criteria for upward two-phase flow in vertical tubes," *International Journal of Heat and Mass Transfer*, vol. 27, pp. 723–737, May 1984.

[13] H. Tsuge, K. Terasaka, W. Koshida, and H. Matsue, "Bubble formation at submerged nozzles for small gas flow rate under low gravity," *Chemical Engineering Science*, vol. 52, no. 20, pp. 3415–3420, 1997.

[14] Techshot, "Multi-use variable-gravity platform." Webpage, Jan. 2019.

[15] A. A. Kulkarni and J. B. Joshi, "Bubble formation and bubble rise velocity in gas-liquid systems: A review," *Industrial & Engineering Chemistry Research*, vol. 44, pp. 5873–5931, Aug. 2005.

[16] C. Herman, S. Change, and E. Iacona, "Bubble detachment in variable gravity under the influence of electric fields," in *ASME International Mechanical Engineering Congress and Exposition*, Dec. 2002.

[17] O. Pamperin and H. Rath, "Influence of buoyancy on bubble formation at submerged orifices," *Chemical Engineering Science*, vol. 50, pp. 3009–3024, 1995.

[18] S. Benner, G. Durback, K. Kolos, and R. Bayt, "A breadboard flight experiment for two-phase flow visualization in microgravity," in *AIAA Meeting Papers*, American Institute of Aeronautics and Astronautics, Jan. 1995.

[19] M. J. Sathe, I. H. Thaker, T. E. Strand, and J. B. Joshi, "Advanced piv/lif and shadowgraphy system to visualize flow structure in two-phase bubbly flows," *Chemical Engineering Science*, vol. 65, pp. 2431–2442, Apr. 2010.

[20] R. Lindken and W. Merzkirch, "A novel piv technique for measurements in multiphase flows and its application to two-phase bubbly flows," *Experiments in Fluids*, vol. 33, pp. 814–825, Dec. 2002.

[21] T. R. Oakley, E. Loth, and R. J. Adrian, "A two-phase cinematic piv method for bubbly flows," *Journal of Fluids Engineering*, vol. 199, no. 3, p. 707, 1997.

[22] D. Bröder and M. Sommerfeld, "Combined piv/ptv-measurements for the analysis of bubble interactions and coalescence in a turbulent flow," *The Canadian Journal of Chemical Engineering*, vol. 81, pp. 756–763, June 2003.

[23] T. R. Nigmatulin, F. J. Bonetto, A. E. Larreteguy, R. T. L. Jr., and J. B. McQuillen, "An experimental study of dispersed liquid/liquid two-phase upflow in a pipe," *Chemical Engineering Communications*, vol. 182, no. 1, pp. 121–162, 2000.

[24] K.-H. Cho, S. Kim, and Y.-J. Lee, "A fast eit image reconstruction method for the two-phase flow visualization," *International Communications in Heat and Mass Transfer*, vol. 26, pp. 637–646, July 1999.

[25] S. Chowdhury, C. Gunes, Q. M. Marashdeh, and F. L. Teixeira, "Fast imaging of velocity profiles of two-phase flows using electrical capacitance volume tomography sensors," in *2017 XXXIInd General Assembly and Scientific Symposium of the International Union of Radio Science (URSI GASS)*, pp. 1–3, URSI, Aug. 2017.

[26] A. Wang, Q. Marashdeh, and L.-S. Fan, "Ecvt imaging of 3d spiral bubble plume structures in gasliquid bubble columns," *The Canadian Journal of Chemical Engineering*, vol. 92, pp. 2078–2087, Dec. 2014.

[27] S. Kim, M. C. Kim, K. Y. Kim, and Y. J. Lee, "Regularization methods in electrical impedance tomography technique for the two-phase flow visualization," *International Communications in Heat and Mass Transfer*, vol. 28, pp. 773–782, Aug. 2001.

[28] T. Xue, L. Qu, Z. Cao, and T. Zhang, "Three-dimensional feature parameters measurement of bubbles in gasliquid two-phase flow based on virtual stereo vision," *Flow Measurement and Instrumentation*, vol. 27, pp. 29–36, 2012.

[29] C. Pfeifer, C. Bruzzese, G. Fast, D. Kuhn, and G. Class, "Application of the tomographic laser doppler anemometry (tdla) to a fuel spray," *Flow Measurement and Instrumentation*, vol. 22, pp. 456–460, 2011.

[30] M. Kim, S. Kim, H. Lee, Y. J., K. Kim, and S. Anghaie, "An experimental study of electrical impedance tomography for the two-phase flow visualization," *International Communications in Heat and Mass Transfer*, vol. 29, no. 2, pp. 193–202, 2002.

[31] Y. Liu, M. Zu, X. Wang, and J.-E. Choi, "Two-phase flow visualization employing gauss-newton method in microchannel," *TELKOMNIKA*, vol. 11, p. 733, Dec. 2013.

[32] D. J. Chato, J. Marchetta, J. I. Hochstein, and M. Kassemi, "Approaches to validation of models for low gravity fluid behavior," in *42nd Aerospace Sciences Meeting and Exhibit*, (Reno, Nevada,), AIAA, Jan. 2004.

[33] K. M. Hurlbert, *Flow dynamics for two -phase flows in partial gravities*. phdthesis, University of Houston, Dec. 2000.

[34] F. Suñol and R. González-Cinca, "Effects of gravity level on bubble formation and rise in low-viscosity liquids," *Physical Review*, vol. 91, no. 5, p. 053009, 2015.

[35] G. Smedley, "Preliminary drop-tower experiments on liquid-interface geometry in partially filled containers at zero gravity," *Experiments in Fluids*, vol. 8, pp. 312–318, Mar. 1990.

[36] J. I. Petty, "Zero-gravity plane on final flight." Webpage, Oct. 2004.

[37] A. Chowdhury, "Mission/study information: Sts-61a." Webpage, Oct. 2018.

[38] A. Agrawal, "Surface tension of polymers." Class Lecture, June 2005.

[39] L. A. Girifalco and R. J. Good, "A theory for the estimation of surface and interfacial energies. i. derivation and application to interfacial tension," *Journal of Physical Chemistry*, vol. 61, pp. 904–909, July 1957.

[40] T. Babadagli, X. Ren, and K. Develi, "Effects of fractal surface roughness and lithology on single and multiphase flow in a single fracture: An experimental investigation," *International Journal of Multiphase Flow*, vol. 68, pp. 40–58, Jan. 2015.

[41] Z. Zhang, "A flexible new technique for camera calibration," *IEEE Transactions on Pattern Analysis and Machine Intelligence*, vol. 22, pp. 1330–1334, Nov. 2000.

[42] Z. Zhang, "Camera calibration with one-dimensional objects," *IEEE Transactions on Pattern Analysis and Machine Intelligence*, vol. 26, pp. 892–899, May 2004.

[43] M. Hodlmoser, H. Zollner, and M. Kampel, "An evaluation of camera calibration methods using digital low cost cameras," in *Computer Vision Winter Workshop*, 2010.

[44] O. Semeniuta, "Analysis of camera calibration with respect to measurement accuracy," *Procedia CIRP*, vol. 41, pp. 765–770, 2016.

[45] S. Yeung and A. Alahi, "Introduction to computer vision." Stanford Artificial Intelligence Laboratory, Webpage, 2015.

[46] A. Zdziennicka, K. Szymczyk, and B. Jaczuk, "Correlation between surface free energy of quartz and its wettability by aqueous solutions of nonionic, anionic and

cationic surfactants," *Journal of Colloid and Interface Science*, vol. 340, pp. 243–248, 2009.

[47] D. Enterprises, ""surface energy data for pc: Polycarbonate, cas 24936-68-3," techreport, Diversified Enterprises, 2009.

[48] J. Narbon, C. Moreno-Diaz, and J. Arenas, "Influence of surface treatment on the surface energy of an aluminum sibstrate," *Colloids and Surfaces*, vol. A, no. 560, pp. 323–329, 2019.

[49] C. Rulison, "Effect of temperature on the surface energy of solids sometimes it does matter," techreport, Kruss, 2005.

[50] D. Enterprises, "Surface energy data for ptfe: Polytetrafluoroethylene, cas 9002-84-0," techreport, Diversified Enterprises, 2009.